

Master thesis:
Magnus force based skyrmionic activation function

Anton Rolf Kettner
Matrikel-Nr.: 7056560
Nanoscience M.Sc.
Universität Hamburg
July 3rd, 2024

1st referee: Prof. Dr. Roland Wiesendanger
2nd referee: Dr. Elena Vedmedenko

Table of Contents

1	Abstract	I
2	Zusammenfassung	II
3	Introduction	1
3.1	Motivation.....	1
3.2	State of the Art.....	2
3.3	Aim	2
4	Theory	3
4.1	Magnetism Basics.....	3
4.1.1.	Magnetic Materials.....	3
4.1.2.	Macroscopic vs. Atomistic Classical Magnetism	4
4.1.3.	Heisenberg Exchange Interaction.....	4
4.1.4.	Dzyaloshinskii-Moriya Interaction.....	6
4.1.5.	Magnetic Anisotropy	7
4.1.6.	Zeeman Interaction	8
4.2	Introduction to Skyrmions	8
4.3	Classical Spin Dynamics	10
4.3.1.	Landau Lifshitz Gilbert Equation.....	10
4.3.2.	LLG Extension with a Spin Torque.....	11
4.3.3.	Thiele Ansatz	12
4.4	Realistic Current Distribution	13
4.5	Machine Learning.....	15
4.5.1.	Fundamental Structure of Artificial Neural Networks.....	15
4.5.2.	Activation Functions and Bias	17
5	Methods	19
5.1	Numerical Techniques.....	19
5.1.1.	Methods for solving the Landau-Lifshitz-Gilbert equation.....	19
5.1.2.	Methods of solving for a realistic current distribution	21
5.1.3.	Method for exact measurement of drift angles.....	22

5.2	Analysis with Thiele type equation	24
6	Relevant Assumptions.....	26
6.1	Simulation Parameters.....	26
6.2	Analysis.....	27
7	Results	28
7.1	Skyrmion creation	28
7.2	Skyrmion edge repulsion	30
7.2.1.	Trajectory of skyrmion due to edge without current	30
7.2.2.	Forces on the skyrmion due to an edge.	32
7.3	Establishing principles for racetrack design	33
7.3.1.	Exploring the trajectory with respect to the β/α relation	34
7.3.2.	Current influenced skyrmion edge interaction	36
7.3.3.	Skyrmion dynamics for realistic current distributions	38
7.4	Designing a skyrmion based ReLU racetrack	41
7.4.1.	Case 1: $\alpha > \beta$	42
7.4.2.	Case 2: $\beta > \alpha$	47
8	Conclusion.....	48
9	Outlook	50
10	Bibliography	52
	Declaration of Academic integrity	58
11	Appendix	59
11.1	Drift speed and angle in relation to the current and β	59
11.2	Derivation of the skyrmion velocity from the Thiele equation	60
11.3	Derivation of $\phi \approx \overline{\phi}_{\text{NN}}$	62

1 Abstract

This thesis investigates the dynamics of magnetic skyrmions in confined nanoscale geometries. We developed two nanowires with theoretical simulations that output a rectified version (ReLU) of the input number of skyrmions for potential implementations in neuromorphic computing. For the simulations, we used the energy-interaction parameters for the dual layer Pd/Fe on Ir(111) with one nanowire design accounting for a negative skyrmion Hall angle ($\beta < \alpha$) and one for a positive skyrmion Hall angle ($\beta > \alpha$).

Furthermore, we explore the current-driven motion of skyrmions in detail. The skyrmion drift is analyzed as a superposition of spin torque transfer by a current ($\vec{\nu}_{\text{STT}}$) and edge repulsion ($\vec{\nu}_{\vec{F}}$) due to confining geometries.

This study also establishes guidelines for racetrack design, considering factors such as corners, pinch points, and the skyrmion Hall angle.

These findings contribute significantly to understanding skyrmion dynamics and their potential applications in spintronics and neuromorphic computing. Our results reveal that further investigations of skyrmion dynamics with non-zero temperatures, the presence of defects, and different current strength regimes would be of great interest.

2 Zusammenfassung

Diese Arbeit untersucht die Dynamik magnetischer Skyrmionen in begrenzten Geometrien. Durch theoretische Simulationen haben wir zwei Nanodrähte entwickelt, die eine nichtlineare Ausgabe (ReLU) aus einer Eingabe von Skyrmionen erzeugen und potenziell im neuromorphen Computing eingesetzt werden können. Während das eine Nanodraht-Design nur für negative Skyrmion Hall Winkel ($\beta < \alpha$) funktioniert, ist das andere Design auf positive Skyrmion Hall Winkel ausgelegt ($\beta > \alpha$). Für alle Simulationen wurden die Spin-Wechselwirkungsparameter von der Doppelschicht Pd/Fe auf Ir(111) verwendet.

Fortführend erforschen wir den Skyrmion Drift aufgrund eines angelegten Stroms. Dabei wird der Skyrmion Drift mithilfe einer Superposition aus strominduzierter Bewegung ($\vec{\nu}_{\text{STT}}$) und Randabstoßung ($\vec{\nu}_{\vec{F}}$) analysiert.

Um einen effizienten Design-Prozess von Nanodrähten zu ermöglichen, etabliert diese Studie Richtlinien für das Design von skyrmionischen Nanodrähten unter Berücksichtigung der Ecken, Verengungen und des Skyrmion Hall Winkels.

Unsere Ergebnisse tragen wesentlich zum Verständnis der Skyrmion-Dynamik sowie ihrer potenziellen Anwendungen in der Spintronik und im neuromorphen Computing bei.

Weiterführende Untersuchungen zu Stromstärkeregimen und Beziehungen zum Skyrmion-Radius sind von Interesse. Zusätzlich könnten Simulationen mit Fehlstellen und realistischen Temperaturen auf die Umsetzbarkeit einer potentiellen experimentellen Studie hindeuten.

3 Introduction

Firstly, we will present our motivation for this work, the current state of the art and the aim of this thesis.

3.1 Motivation

In many areas of human life, computers have gained more and more importance, including work, communication, entertainment, and education. Over the last few years, AI applications have revolutionized our perception of computers as simple machines that can do specific tasks in predictable ways. Increasingly powerful GPU chips have enabled deep learning of large language models on a different scale than before. Due to globalization, the public's adaptation to such new technologies has become incredibly fast. When OpenAI made GPT-3.5 publicly available for free in November 2022, 1 million users adopted this new technology in only five days.^{1,2}

To the present day, all AI applications run on locally owned hardware or in big data centers but still use traditional von Neumann architectures with inherent efficiency limitations.^{3–5}

One strategy to overcome these limitations is known as deep modular design. I.e., nanoscale devices optimize essential computational steps necessary for the specific application. The fundamental idea is that these devices can interconnect into different, more sophisticated products with existing von Neumann hardware or other devices. Particularly promising for the development of these devices are the ones utilizing the dynamics of magnetic moments on a microscale, i.e., spintronics.

Several papers have been published over the past years, implementing the functionality of neurons or synapses into this spintronics framework.^{6–10} Even though these devices demonstrate the proposed functionality, they lack connectivity to each other. Therefore, the potential for implementation into a more extensive artificial neural network (ANN) based on spintronics is limited. They must be read out with traditional hardware and set to specific values separately each time.

Here, we propose utilizing the intrinsic interactions of small magnetic knots (skyrmions) to achieve a controllable non-linear output (ReLU), essential for modern deep ANNs. This design could be integrated into a larger scale, purely spintronics-based ANN, avoiding any connection by traditional hardware.

3.2 State of the Art

In the realm of spintronics, skyrmions have been a hot topic for over a decade now.^{11–13} They are small and mobile magnetic knots, so far only observed in ferromagnets, drifting across magnetic surfaces with comparatively low currents.^{14,15}

Skyrmions have been proposed as potential replacements for various applications, including temporary information storage, transistors, and mimicking different gates.^{6,16–18} They are primarily propelled along a nanowire (racetrack) due to current injection. This current induces a spin-torque, moving magnetic configurations across the surface.¹⁷

Skyrmion annihilation, a critical concern for device reliability, has been investigated by multiple groups, including the effect of rough edges or impurities¹⁹ and at the inner edges of racetrack bends.²⁰ Multiple other groups have proposed different ways to avoid annihilation, e.g., tuning the local anisotropy^{20,21} or countering the skyrmion Hall effect.^{22,23} This effect is proportional to the non-adiabatic portion of the spin-torque. For domain wall movement via spin-torque, several experimental studies have reported high degrees of non-adiabaticity (β) in several materials.^{24–26} Even though, only Jiang et al.²⁷ experimentally observed a drift indicating a negative skyrmion Hall angle ($\beta > \alpha$) in, the value seems to overlap with domain wall movement in similar materials. The interplay between skyrmion Hall angle, edge effects, and material parameters remains an area of ongoing investigation.

One reason for the skyrmions' image as quasiparticles is their intrinsic repulsion, not only from each other but also from the edges of the ferromagnetic surface. The effects of this repulsion on the drift velocity of skyrmions along a racetrack have been studied widely when a current propels them forward.^{28,29}

In [30] an extra term is added to the Thiele equation by Martinez et al. when investigating edge repulsion. We contacted him for more information because some of our results directly collided with Fig. 3 in Martinez's publication. It seems like more research is required to verify his proposed extra term with simulations.

3.3 Aim

Despite the significant progress in understanding skyrmion dynamics, several key areas remain unexplored or poorly understood. Investigations of skyrmion-edge repulsion and its implications for racetrack design without separation from a driving force remain limited. This gap in knowledge presents an opportunity to develop more efficient and reliable skyrmion-based devices.

Moreover, the interplay between material parameters (such as the β/α ratio), race-track geometry, and skyrmion behavior offer parameter space for optimization. Exploring this space could lead to the design of more efficient and versatile skyrmion-based devices.

Due to its simplicity and effectiveness, the ReLU (Rectified Linear Unit) function is a commonly used activation function in modern neural networks. Implementing a ReLU function using skyrmions could yield more energy-efficient neural network hardware, motivating our investigation into designing a skyrmionic ReLU racetrack. This racetrack could serve as a building block for future neuromorphic devices.³¹

This thesis aims to address these gaps in our understanding, focusing on the edge repulsion of skyrmions and its implications for racetrack design and functionality. By doing so, we hope to contribute to developing more advanced skyrmion-based computational elements and push forward the field of skyrmion-based spintronics.

4 Theory

4.1 Magnetism Basics

Magnetism has intrigued mankind for centuries, with early observations tracing back to ancient Greece and China.³² Despite the classical understanding provided by Maxwell's equations, the quantum mechanical nature of magnetism, especially the formation of permanent magnets, remained obscure until modern physics elucidated it.³³ This chapter focuses on a basic understanding of magnetism, its connection to the atomic-scale magnetic moments of atoms, and the underlying interactions that govern these phenomena.

4.1.1. Magnetic Materials

The five primary categories of magnetic materials (diamagnets, paramagnets, ferromagnets, antiferromagnets, and ferrimagnets) are illustrated in Fig. 1 with their respective intrinsic alignment of atomic spins.

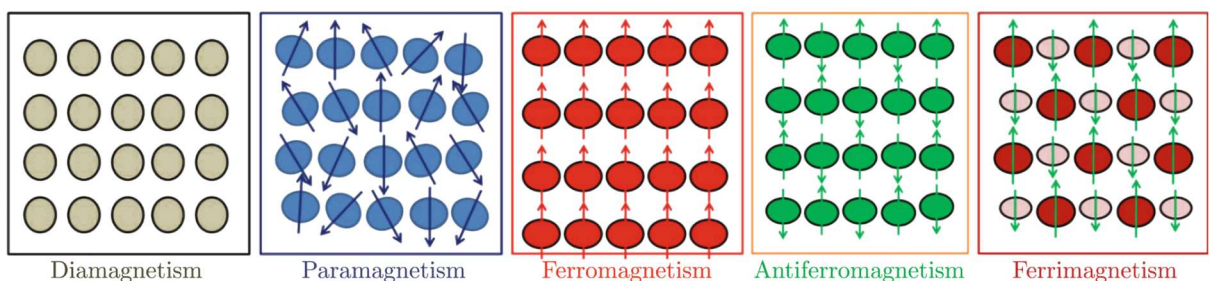


Fig. 1 Alignment of atomic spins (arrows) for the five primary types of magnetism: diamagnetism, paramagnetism, ferromagnetism, antiferromagnetism, and ferrimagnetism (adapted from [34]).

These types are generally classified by their magnetic susceptibility,

$$\chi = \frac{M}{H}, \quad (1)$$

which measures the material's magnetization M in response to an external magnetic field H . Diamagnetic materials possess a small negative susceptibility, while paramagnetic substances demonstrate a slight positive susceptibility. In paramagnetic materials, the magnetic moments are randomly oriented, yielding an overall magnetization of zero, as illustrated in Fig. 1. Ferromagnetic materials, on the other hand, have a notable positive susceptibility due to their aligned magnetic moments, which leads to a considerable overall magnetization. Antiferromagnetic materials exhibit a small positive susceptibility with magnetic moments aligned antiparallel, nullifying each other and resulting in no net magnetization. Ferrimagnets feature two antiparallel magnetic sublattices. As the magnetic moments are not the same in each sublattice, the result is a notable net magnetization akin to the magnetization of ferromagnets, marked by a high positive susceptibility.^{34,35}

4.1.2. Macroscopic vs. Atomistic Classical Magnetism

The macroscopically observable magnetism is governed by the collective alignment of atomic-scale magnetic moments within a material. Macroscopic properties such as magnetization and magnetic susceptibility, mentioned in the previous chapter arise from complex interactions at the atomic level. These properties become evident when magnetic domains - regions where atomic magnetic moments are aligned - are large enough to produce a detectable magnetic field.³⁴

At the atomic level, magnetism originates from the magnetic moments associated with electrons. These moments arise from two primary sources: the electron's spin and its orbital movement around the nucleus. The intrinsic spin in materials with unpaired electrons leads to a substantial atomic magnetic moment in space. Summing over the spins of unpaired electrons leads to an atomic spin or magnetization (\vec{S}). These spins interact with each other based on local energy minimization. The energies for these interactions are described by Hamiltonians and presented in the upcoming chapters of 4.1.

4.1.3. Heisenberg Exchange Interaction

The Heisenberg exchange interaction is fundamental to our understanding of magnetic ordering in materials. Introduced by Werner Heisenberg in 1928,^{36,37} it describes how the

quantum mechanical properties of electrons, primarily stemming from their spin states, can lead to the magnetic alignment of atoms. The exchange interaction is a quantum phenomenon arising from the competition between the Coulomb energy and the Pauli exclusion principle. The principle dictates that no two electrons can simultaneously occupy the same quantum state, which increases the Coulomb energy, forcing the electrons to occupy excited one-electron states.³⁸ Thermal energy can disrupt this delicate balance. As temperature rises above the Curie temperature T_C , thermal excitations provide enough energy to overcome the exchange interaction, causing the magnetic order to collapse - a phase transition occurs from a magnetically ordered state to a disordered, paramagnetic state.^{35,36}

To describe this mathematically, we can model the system with N classical spins denoted by \vec{S}_i with $i \in [1, N]$. The exchange energy can be expressed with the exchange Hamiltonian $\mathcal{H}_{\text{exch}}$ in terms of the exchange tensor \vec{J}_{ij} as:³⁵

$$\mathcal{H}_{\text{exch}} = - \sum_{i \neq j, i < j}^N \vec{S}_i \cdot \vec{J}_{ij} \cdot \vec{S}_j = - \sum_{i \neq j, i < j}^N \left[\sum_{a,b=x,y,z} S_i^a \cdot J_{ij}^{ab} \cdot S_j^b \right]. \quad (2)$$

The exchange tensor for the interaction between spins \vec{S}_i and \vec{S}_j can be decomposed into three distinct components:

$$\vec{J}_{ij} = J_{ij} \cdot \mathbb{1} + \vec{J}_{ij}^s + \vec{J}_{ij}^a. \quad (3)$$

Here, J_{ij} signifies the isotropic part of the exchange tensor, \vec{J}_{ij}^s denotes the symmetric anisotropic exchange, \vec{J}_{ij}^a refers to the antisymmetric exchange, and $\mathbb{1}$ represents the unit tensor. These isotropic, symmetric, and antisymmetric interactions can be obtained from the \vec{J}_{ij} with:

$$J_{ij} = \frac{1}{3} \cdot \text{tr}(\vec{J}_{ij}) ; \quad \vec{J}_{ij}^s = \frac{\vec{J}_{ij} + \vec{J}_{ij}^T}{2} - J_{ij} \cdot \mathbb{1} ; \quad \vec{J}_{ij}^a = \frac{\vec{J}_{ij} - \vec{J}_{ij}^T}{2}, \quad (4)$$

where \vec{J}_{ij}^T is the transpose of \vec{J}_{ij} . The isotropic exchange stemming from J_{ij} is also referred to as the Heisenberg exchange. It was initially introduced to explain the spin ordering at low temperatures:³⁶

$$\mathcal{H}_{\text{Heisenberg}} = - \sum_{i \neq j, i < j}^N J_{ij} \cdot \vec{S}_i \cdot \vec{S}_j. \quad (5)$$

Depending on the sign of the exchange interaction, one can observe either ferromagnetic order for positive J_{ij} or antiferromagnetic order for negative J_{ij} . In the former case, spins align parallelly, as explained by the Heisenberg theory of ferromagnetism.³⁶ In the latter case, the antiparallel alignment of spins corresponds to Néel's theory of antiferromagnetism.³⁹ The Heisenberg exchange tends to be stronger than the other interactions described in the following chapters.³⁵

In our simulations, the spins are replaced with their normalized magnetization vectors \vec{n} ,

$$\vec{n} = \vec{S}/\mu_s, \quad (6)$$

and only neighboring interactions are considered. As we model a perfect two-dimensional hexagonal lattice, the Hamiltonian for our Heisenberg exchange interaction reads,

$$\mathcal{H}_{\text{ex}} = -\frac{1}{2} \cdot J \cdot \sum_{\vec{r}}^N \sum_{\vec{g}}^{N_{\text{NN}}} [\vec{n}(\vec{r}) \cdot \vec{n}(\vec{r} + \vec{g})], \quad (7)$$

summing over all lattice sites \vec{r} . The other sum is over the NN-vectors ($\equiv \vec{g}$) pointing toward all next neighbors ($N_{\text{NN}} = 6$). J can be used as the interaction constant because J_{ij} is the same for all NN interactions.

4.1.4. Dzyaloshinskii-Moriya Interaction

The antisymmetric exchange, also called Dzyaloshinskii-Moriya (DM) interaction, arises from \vec{J}_{ij}^a considering strong spin-orbit coupling (SOC) in an environment lacking inversion symmetry. It was first proposed by Igor Dzyaloshinskii in 1958⁴⁰ and linked to SOC by Toru Moriya in 1960.⁴¹

The Hamiltonian capturing the antisymmetric exchange between two spins \vec{S}_i and \vec{S}_j is given by:

$$\mathcal{H}_{\text{DMI}} = \vec{D}_{ij} \cdot (\vec{S}_i \times \vec{S}_j). \quad (8)$$

The \vec{D}_{ij} vector can be expressed with the antisymmetric part of the exchange tensor as,⁴²

$$\vec{D}_{ij} = \frac{1}{2} \cdot \begin{pmatrix} J_{ij}^{yz} - J_{ij}^{zy} \\ J_{ij}^{zx} - J_{ij}^{xz} \\ J_{ij}^{xy} - J_{ij}^{yx} \end{pmatrix}, \quad (9)$$

and can be calculated using *ab initio* methods.

For skyrmionic systems in a magnetic monolayer k

$$\vec{D}_{ij}^k = D^k \cdot (\vec{e}_z \times \vec{u}_{ij}^k), \quad (10)$$

where \vec{e}_z and \vec{u}_{ij} point along the z direction and from site i to j , respectively. The DM interaction plays an essential role as it can produce exotic magnetization textures, such as skyrmions, that have the potential to be used in magnetic memories or for computational structures.³⁵

Applied to our simulation of a 2D hexagonal plane, the DM Hamiltonian reads:

$$\mathcal{H}_{\text{DM}} = \frac{1}{2} \cdot \sum_{\vec{r}}^N \sum_{\vec{g}}^{N_{\text{NN}}} \vec{D}_{\vec{g}} \cdot [\vec{n}(\vec{r}) \times \vec{n}(\vec{r} + \vec{g})]. \quad (11)$$

4.1.5. Magnetic Anisotropy

Magnetocrystalline anisotropy induces spins to orient themselves along a specific lattice direction, known as the easy axis. Anisotropy stems from the interaction between spin crystal lattice and is facilitated by spin-orbit coupling. Typically, materials present either uniaxial anisotropy or cubic anisotropy, which are characterized by their respective Hamiltonians.³⁵

$$\mathcal{H}_{\text{aniso}}^{\text{u}} = - \sum_i^N k_{\text{u}} \cdot (\vec{S}_i \cdot \vec{e})^2, \quad (12)$$

$$\mathcal{H}_{\text{aniso}}^{\text{c}} = - \sum_i^N [k^1 (S_x^2 S_y^2 + S_y^2 S_z^2 + S_x^2 S_z^2) + k^2 (S_x^2 S_y^2 S_z^2) + \dots]. \quad (13)$$

Here, \vec{S}_i represents the spin vector, k_{u} stands for the first-order uniaxial anisotropy constant, and \vec{e} denotes the easy axis direction, which is \vec{e}_z in our simulations. In eq. (13) the first two terms of the expansion for cubic anisotropy are presented, with the components of the magnetic moments S_x , S_y , S_z .³⁵

Considering that we model a 2D lattice spanning across the x- and y-axis, we use the following Hamiltonian for a uniaxial anisotropy, favoring a z-orientation for the magnetization direction \vec{n} with a positive k_u :

$$\mathcal{H}_{\text{an}}^u = -k_u \cdot \sum_{\vec{r}}^N [n_z(\vec{r})]^2. \quad (14)$$

4.1.6. Zeeman Interaction

The Zeeman energy represents the interaction of atomic moments with an external magnetic field, which manifests as a magnetic torque capable of reversing the magnetization direction. This interaction, formally referred to as the Zeeman energy, is mathematically expressed as follows:^{35,43}

$$\mathcal{H}_{\text{Zee}} = - \sum_i^N \vec{S}_i \cdot \vec{B}_{\text{ext}} \quad (15)$$

The atomic spins align parallel to the magnetic field to reduce the total energy. Analogous to eq. (7), (11) and (14),

$$\mathcal{H}_{\text{Zee}} = - \sum_{\vec{r}}^N \vec{B}(\vec{r}) \cdot \vec{n}(\vec{r}), \quad (16)$$

with \vec{B} being the, with μ_s (magnetic moment of a single atomic spin) normalized energy of the external magnetic field ($\vec{B} = \mu_s \cdot \vec{B}_{\text{ext}}$).

4.2 Introduction to Skyrmions

Skyrmions are topologically protected stable configurations within certain materials' magnetic structures. First theoretically proposed by the British physicist Tony Skyrme in the framework of field theory,⁴⁴ skyrmions remained relatively obscure until recent decades when experimental advances allowed for their observation in magnetic materials. Their discovery and ensuing popularity especially took off around 2009, when skyrmion lattices were first experimentally observed in bulk MnSi,¹¹ and afterward, individual chiral skyrmions were found in Pd/Fe on Ir(111).^{13,45}

Skyrmions typically emerge due to large DMI-vectors either in bulk materials with non-centrosymmetric crystal structures or in thin films, e.g., depositing a heavy metal

layer on top of a ferromagnetic layer to induce strong SOC.⁴⁶ Skyrmions are localized magnetic configurations, forming a vortex-like structure and can be categorized using the vorticity m and helicity γ :¹⁹

$$(\varphi) = m \cdot \varphi + \gamma. \quad (17)$$

The topological skyrmion number N_{Sk} is also an important parameter combining the vorticity ($m \in \{-1, 1\}$) with the direction of the skyrmion's core $n_z^{r=0}$ in the relation:¹²

$$N_{\text{Sk}} = -m \cdot n_z^{r=0}. \quad (18)$$

In Fig. 2, the most relevant skyrmion structures with $N_{\text{Sk}} = \{-1, 1\}$ can be observed, together with a depiction of eq. (17).

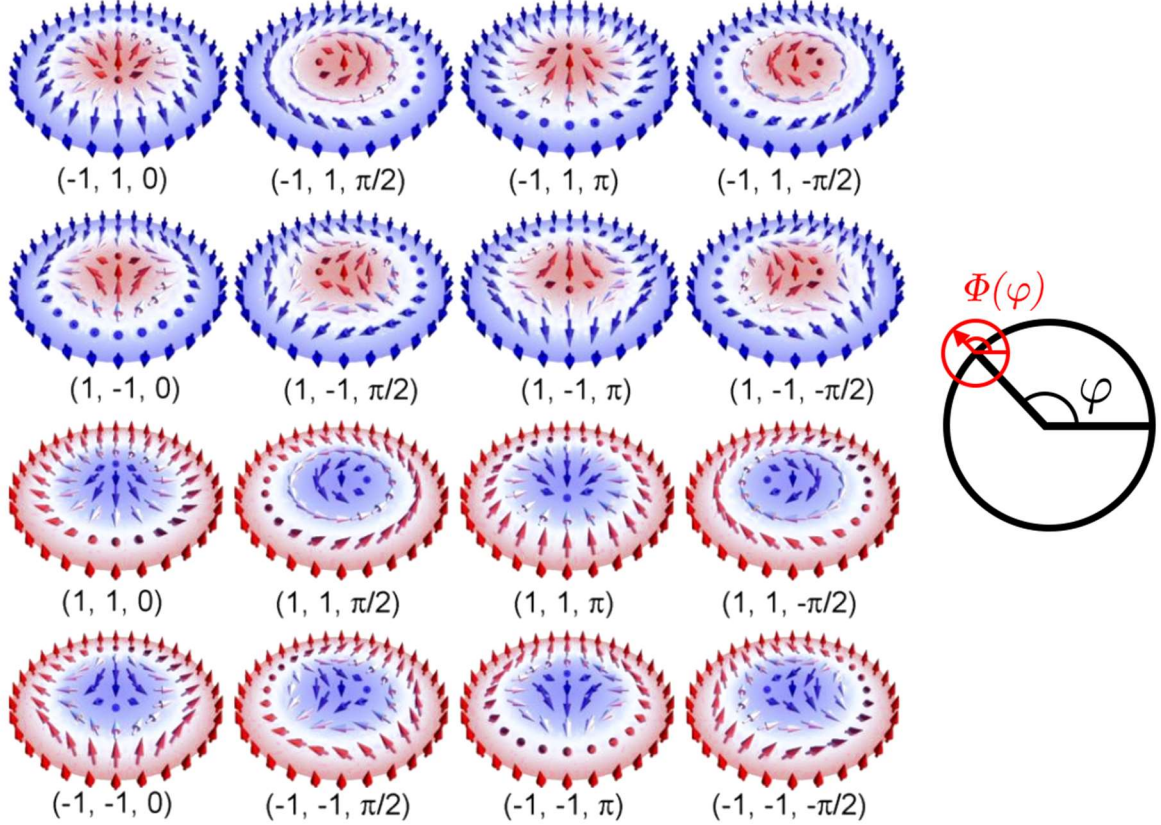


Fig. 2 Illustration of basic skyrmion structures with $(N_{\text{Sk}}, m, \gamma)$ adapted from Zhang et al.¹⁸ By overlaying the sketch on the right with a skyrmion, one can observe the spin being angled toward $\Phi(\varphi)$ at every angle from the center φ (adapted from [19]).

A skyrmion's size and shape can be analyzed with,^{47,48}

$$\Theta_{\text{dw}}(r) = 2 \cdot \arctan \left[\frac{\sinh \left(\frac{r_{\text{Sk}}}{w_{\text{Sk}}} \right)}{\sinh \left(\frac{r}{w_{\text{Sk}}} \right)} \right], \quad (19)$$

describing the polar angle Θ_{dw} of the local magnetization, starting from the skyrmion's center. This equation assumes the skyrmion to have the shape of a 360 ° domain wall. r_{Sk} is interpreted as the skyrmion radius and w_{Sk} as its wall width.

As Θ_{dw} can directly be derived from every spin's z-component eq. (19) can be fitted with each spin's distance from the skyrmion's center r and polar angle Θ_{dw} to obtain r_{Sk} and w_{Sk} .

4.3 Classical Spin Dynamics

The interaction dynamics of magnetic moments with each other are typically described using the Landau-Lifshitz-Gilbert (LLG) equation. We will make use of the normalized local magnetic moment \vec{n} at each atomic site defined by eq. (6).

4.3.1. Landau Lifshitz Gilbert Equation

The LLG equation is derived from the atomistic model of spin dynamics (ASD) based on the Heisenberg Hamiltonian. When modeling a 2D ferromagnetic layer atomically, its implicit Gilbert form for our system reads:⁴⁹⁻⁵²

$$\partial_t \vec{n} = -\gamma \cdot \vec{n} \times \vec{H}_{\text{eff}} + \alpha \cdot \vec{n} \times \partial_t \vec{n}. \quad (20)$$

This equation relates the change of the local magnetization over time $\partial_t \vec{n}$ with the local magnetization \vec{n} under the influence of the effective magnetic field \vec{H}_{eff} . α is the dimensionless Gilbert-damping constant and γ is the gyromagnetic ratio:³²

$$\gamma = \frac{g \cdot \mu_B}{\hbar}. \quad (21)$$

When assuming that μ_s is the same for every atom, we can reformulate eq. (20) into its explicit version by applying the Grassmann identity:

$$\partial_t \vec{n} = -\frac{\gamma}{1 + \alpha^2} \cdot [\vec{n} \times \vec{H}_{\text{eff}} + \alpha \cdot \vec{n} \times (\vec{n} \times \vec{H}_{\text{eff}})]. \quad (22)$$

The explicit version simplifies calculations of the time-evolution of the magnetization texture on our sample over time. The local effective magnetic field \vec{H}_{eff} can be calculated from the Hamiltonians introduced in the previous chapter with:^{19,49}

$$\vec{H}_{\text{eff}} = \frac{1}{\gamma} \left\langle \frac{\partial \mathcal{H}_{\text{tot}}}{\partial \vec{S}} \right\rangle = -\frac{1}{\mu_s} \cdot \partial_{\vec{n}} \mathcal{H}_{\text{tot}}. \quad (23)$$

As only the local \vec{H}_{eff} is required, we can include all of the local Hamiltonians from eq. (7), (11), (14), and (16) into \mathcal{H}_{tot} , omitting only the sums over all lattice sites, to formulate a single equation for \vec{H}_{eff} :

$$\begin{aligned} \vec{H}_{\text{eff}} = & \frac{J}{2 \cdot \mu_s} \cdot \sum_{\vec{g}}^{N_{\text{NN}}} \vec{n}(\vec{r} + \vec{g}) \\ & + \frac{1}{2 \cdot \mu_s} \cdot \sum_{\vec{g}}^{N_{\text{NN}}} \vec{D}_{\vec{g}} \times \vec{n}(\vec{r} + \vec{g}) \\ & + \frac{2 \cdot k_u \cdot \vec{n} \cdot \vec{e}_z}{\mu_s} \\ & + \vec{B}_{\text{ext}}. \end{aligned} \quad (24)$$

4.3.2. LLG Extension with a Spin Torque

As the LLG-equation does not include the dynamics when an in-plane spin polarized current is applied, Bazaliy et al.⁵³ extended the implicit LLG equation of eq.(20). This extension term that can be derived from the adiabaticity assumption,⁴⁹ as conduction electrons adjust their spin orientation when they traverse the magnetic sample. The resulting equation is:

$$\partial_t \vec{n} = -\gamma \cdot \vec{n} \times \vec{H}_{\text{eff}} + \alpha \cdot \vec{n} \times \partial_t \vec{n} - (\vec{v}_s \cdot \nabla) \vec{n}. \quad (25)$$

\vec{v}_s is the velocity of the conduction electrons, defined by,

$$\vec{v}_s = \frac{p \cdot A \cdot h}{2e} \cdot \vec{j}_c, \quad (26)$$

with the polarization p , the surface area A of one Wigner-Seitz-cell, the atomic layer height h , and the current density \vec{j}_c .

Zhang and Li⁵⁴ refined the approach by Bazaliy et al.⁵³ and calculated the magnetization dynamics for a system in which the electrons do not follow the magnetization adiabatically. Their calculations are founded on the spin continuity equation of the itinerant conduction electrons leading to a second so-called β -term. This term arises from the dissipative coupling between conduction electrons and magnetic moments due to non-adiabatic effects.⁵⁵ Their derived equation is:

$$\partial_t \vec{n} = -\gamma \cdot \vec{n} \times \vec{H}_{\text{eff}} + \alpha \cdot \vec{n} \times \partial_t \vec{n} - (\vec{v}_s \cdot \nabla) \vec{n} + \beta \vec{n} \times (\vec{v}_s \cdot \nabla) \vec{n}. \quad (27)$$

Converted into an explicit format, we obtain,

$$\partial_t \vec{n} = \frac{1}{1 + \alpha^2} \cdot \begin{pmatrix} \gamma \cdot (\vec{n} \times \vec{H}_{\text{eff}}) + \alpha \cdot \gamma \cdot \vec{n} \times (\vec{n} \times \vec{H}_{\text{eff}}) \\ -(\alpha\beta + 1)[(\vec{v}_s \cdot \vec{\nabla}) \vec{n}] + (\beta - \alpha) \vec{n} \times [(\vec{v}_s \cdot \vec{\nabla}) \vec{n}] \end{pmatrix}, \quad (28)$$

the LLG equation extended by the so-called Spin-Transfer Torque (STT).⁵⁵

4.3.3. Thiele Ansatz

Thiele⁵⁶ introduced a framework that quantitatively describes a skyrmion's dynamics with a force equilibrium. He derives a linear equation of motion⁵⁰ by projecting the implicit LLG equation onto the corresponding translational modes.⁵⁷ Assuming the skyrmion to be a rigid object, the gyro-coupling vector \vec{G} , the Dissipation Tensor \vec{D} and the Gilbert Damping constant α are used to relate the skyrmions drift velocity $\vec{\nu}$ to an external force \vec{F} with:

$$\vec{G} \times \vec{\nu} + \alpha \vec{D} \cdot \vec{\nu} + \vec{F} = 0. \quad (29)$$

If the sample is exposed to an in-plane spin polarized current, magnetic structures are affected by a STT (s. chapter 4.3.2) described by \vec{v}_s and the non-adiabaticity parameter β . Then eq. (29) can then be extended to:^{30,58}

$$\vec{G} \times (\vec{\nu} - \vec{v}_s) + \vec{D} \cdot (\alpha \vec{\nu} - \beta \vec{v}_s) + \vec{F} = 0. \quad (30)$$

The gyration vector is directly dependent on the geometry of the sample. Assuming an x-y-surface that the skyrmion moves along, the gyration vector's x and y components are 0, therefore \vec{G} can be simplified into,

$$\vec{G} = G \cdot \vec{e}_z, \quad (31)$$

with⁵⁶ $G = N_{\text{Sk}} \cdot \frac{4\pi}{\gamma} \cdot (M_s \cdot h)$. Here N_{Sk} is the skyrmion number,¹² $M_s \cdot h$, i.e., the saturation magnetization times the film's thickness, defines the amount of magnetization per surface area and γ is the gyromagnetic ratio.

As we use an atomic model, the magnetization per surface area is instead defined by μ_s / A_{hex} , with μ_s as the atomic magnetic moment and A_{hex} being the surface area of the hexagonal unit cell in the 2D lattice that we look at, leading to the expression for G :

$$G = N_{\text{Sk}} \cdot \frac{4\pi}{\gamma} \cdot (\mu_s \cdot A_{\text{hex}}) = \frac{2\sqrt{3}\pi \cdot N_{\text{Sk}} \cdot \mu_s \cdot a^2}{\gamma}. \quad (32)$$

As the dissipation tensor is symmetric with $D_{xy} = D_{yx}$, it can be diagonalized by rotating the coordinate system so that the eigenvalues are at $D_{xx} = D_{yy} = D$:²³

$$\overleftrightarrow{\mathbf{D}}_{i,j} = \begin{pmatrix} D & 0 & 0 \\ 0 & D & 0 \\ 0 & 0 & 0 \end{pmatrix}. \quad (33)$$

When the expressions in eq. (31) and eq. (33) are inserted into eq. (30), the outcoming vector equation can be separated into two equations, which can then be solved for ν_x and ν_y (s. chapter 11.1). Written as a vector format the outcome is,

$$\vec{\nu} = \frac{1}{G^2 + \alpha^2 D^2} \cdot \begin{pmatrix} -\alpha D \vec{F} + \vec{G} \times \vec{F} \\ +(G^2 + \alpha \beta D^2) \cdot \vec{v}_s + D(\alpha - \beta) \cdot \vec{G} \times \vec{v}_s \end{pmatrix}, \quad (34)$$

relating the D and \vec{G} directly to a skyrmion's drift velocity by an external force and current.

4.4 Realistic Current Distribution

When dealing with more intricate racetrack designs and STT, the current distribution inside the 2D ferromagnetic layer is no longer a homogenous x-current. To obtain a realistic current distribution, one can reformulate the original problem of “solving for the current distribution” to “finding each local electrical potential” ϕ and then derive the current distribution from Ohm's law:

$$\vec{j} = \sigma \cdot \vec{E} = -\sigma \cdot \vec{\nabla} \cdot \phi . \quad (35)$$

To obtain the local electrical potential ϕ for every atomic site, we can write down equations that must be obeyed everywhere in the system. The continuity equation,

$$\frac{\partial \rho}{\partial t} + \vec{\nabla} \cdot \vec{j}_c = 0, \quad (36)$$

the relation between electrical field \vec{E} and electrical potential ϕ ,

$$\vec{E} = -\vec{\nabla} \phi, \quad (37)$$

and Gauss-law:

$$\vec{\nabla} \cdot \vec{E} = \frac{\rho}{\epsilon_0}. \quad (38)$$

Inserting eq. (37) into (38), we obtain the Poisson equation:

$$\Delta \phi = -\frac{\rho}{\epsilon_0}. \quad (39)$$

We assume that our system does not contain free charges ($\rho = 0$). This assumption leads to simplified variations of the continuity equation,

$$\vec{\nabla} \cdot \vec{j}_c = 0, \quad (40)$$

and the Laplace equation from the Poisson equation:^{59,60}

$$\Delta \phi = 0. \quad (41)$$

With the Laplace equation, we can calculate the electrical potential by assuming the surrounding material to be non-conductive and relaxing using the method described in chapter 5.1.2.

4.5 Machine Learning

Machine Learning (ML) is a broad field within artificial intelligence that focuses on developing algorithms and models that enable computers to learn based on data without being explicitly programmed.⁶¹ ML has gained significant importance due to its wide range of applications across various domains, such as healthcare, finance, marketing, and more. It has been used for stock price prediction, gene-gene interaction detection, energy-related applications, and even in self-adaptive systems.⁶²⁻⁶⁵ The ability of ML algorithms to analyze large data sets and extract valuable insights has revolutionized industries by enabling automation, prediction, and optimization.

The field of ML can be split into three sub-categories depending on the input type: supervised learning, unsupervised learning, and reinforcement learning.⁶¹ Supervised learning involves training a model on labeled data. Here the algorithm learns to map input data to the correct output. On the other hand, unsupervised learning deals with unlabeled data, aiming to discover hidden patterns or structures within the data. Reinforcement learning focuses on training agents to make sequential decisions by rewarding desired behaviors and punishing undesired ones.

In the historical context of ML, significant developments have shaped the field into what it is today. ML has continuously evolved from its early roots in the 1950s with the introduction of neural networks, to the resurgence of interest in the 2010s with the advent of deep learning and big data.⁶¹ Key milestones include the development of decision trees, support vector machines, and, more recently, the breakthroughs in deep learning with neural networks, convolutional neural networks, and recurrent neural networks. One significant recent development in ML is using a Rectified Linear Unit (ReLU) activation function, which has become an essential step in improving the training of deep neural networks.⁶⁶

4.5.1. Fundamental Structure of Artificial Neural Networks

Artificial Neural Networks (ANNs), a subset of algorithms within the domain of ML, are the core of modern ML tools. Their structure of interconnected neurons inside a layered architecture is inspired by the mechanisms inside the human brain. It excels at approximating complex non-linear functions, making ANNs valuable in various applications.

An ANN consists of interconnected nodes, called neurons, inside of multiple layers. These neurons can hold numbers, which are called activations. The input data is converted to a single vector to enable processing by an ANN. This vector contains all the activations of the neurons inside the first layer. The activations from the input layer

travel through the neural network toward the output layer. To achieve the desired behavior of a network, we can tune how the activations propagate through the network from one layer to the next. We will look at how activations propagate through a network to understand the parameters we can tune.⁶⁷

Each neuron activation is calculated by connecting it to all the neurons in the previous layer. A weight is assigned to every one of those connections. Weights are just numbers, controlling how much one neuron is influenced by each neuron in the previous layer. To obtain the activation of a neuron, we sum up all activations of neurons from the previous layer using the respective weights for the connections. Repeating this weighted summation starting from the first and ending at the last layer gives us the output vector. An illustration of this so-called ANN architecture with one hidden layer with three neurons and an input/output layer consisting of 5 neurons each is seen in Fig. 3.

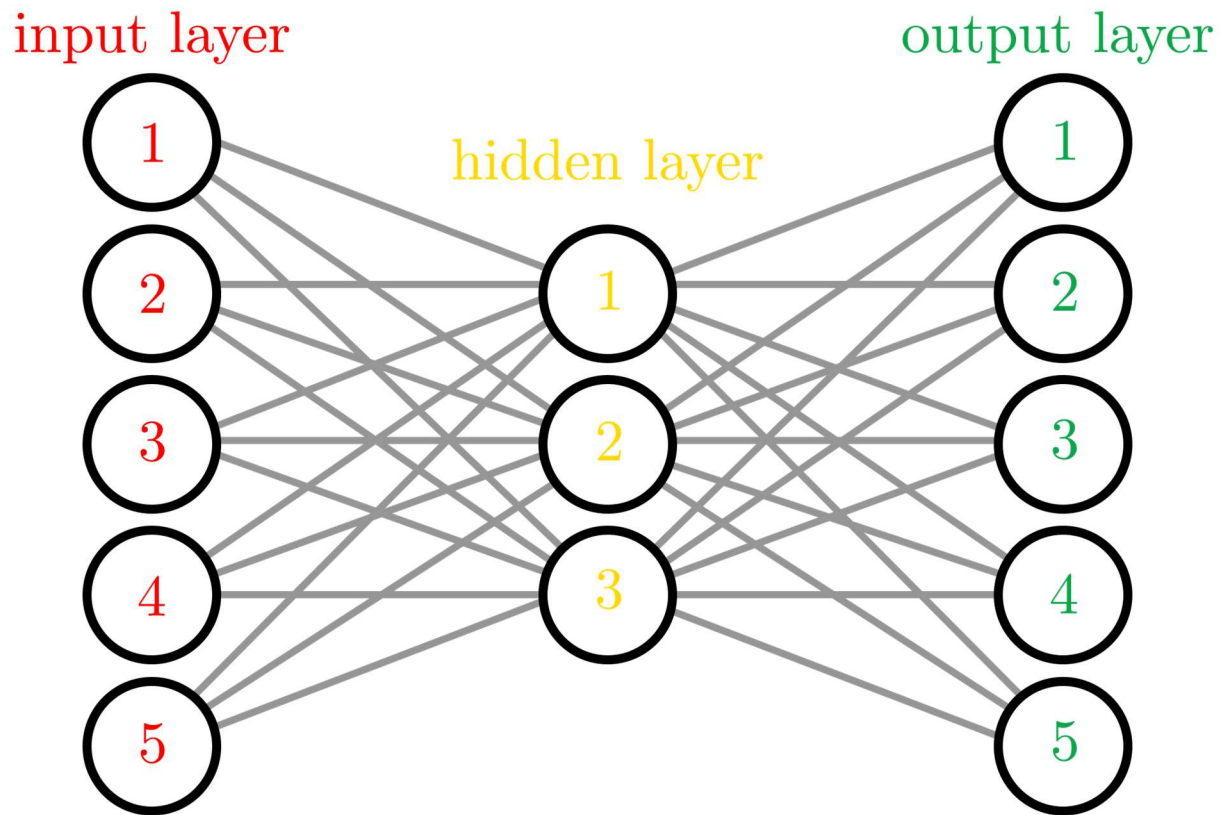


Fig. 3 Exemplary architecture of a small ANN with one hidden layer. Black circles illustrate the neurons, and the weights (gray lines) connect the neurons. The input layer's neurons are numbered in red, the hidden layer's neurons in yellow, and the output layer's neurons in green.

Mathematically, it is easier to represent the sum of all weighted activations with the weights inside a matrix named $\vec{W}_{n,m}$, being multiplied with the vector \vec{a}_n , containing all neuron activations of the previous layer. n is the number of neurons inside the

previous layer, and m the number of neurons in the current layer. The vector \vec{a}_m represents all activations in the new layer and can be calculated via:

$$\vec{a}_m = \vec{W}_{n,m} \cdot \vec{a}_n. \quad (42)$$

4.5.2. Activation Functions and Bias

So far the described model has been a simple linear regression. The final vector could be calculated with a single matrix multiplication. To mimic a real neural network, we must introduce non-linearity with a function ϕ , wrapping the expression in eq. (43) to calculate the activations inside the next layer. E.g., the sigmoid function,

$$\sigma(x) = \frac{1}{1 + \exp(-x)}, \quad (43)$$

can be used, wrapping the right side of eq. (42) and mapping all inserted numbers (s. eq. (42)) to the range [0,1],

$$\vec{a}_m = \phi(\vec{W}_{n,m} \cdot \vec{a}_n), \quad (44)$$

similar to the way neurons are connected inside a brain. It has been proven for ANNs to learn much more efficiently if a bias b can shift the entire weighted sum function to the left or right.⁶⁸ This can be written in a vector format with \vec{b}_n as well:

$$\vec{a}_m = \phi(\vec{W}_{n,m} \cdot \vec{a}_n - \vec{b}_n). \quad (45)$$

With non-linear functions and bias parameters, ANNs can approximate a wide range of functions, enabling the network to learn complex patterns and relationships in data. The choice of activation function is not apparent. Popular activation functions also include tanh- and ReLU-functions,

$$\tanh(x) = \frac{\exp(x) - \exp(-x)}{\exp(x) + \exp(-x)}, \quad (46)$$

$$\text{ReLU}(x) = \max(0, x), \quad (47)$$

which are compared to the sigmoid function in Fig. 4.

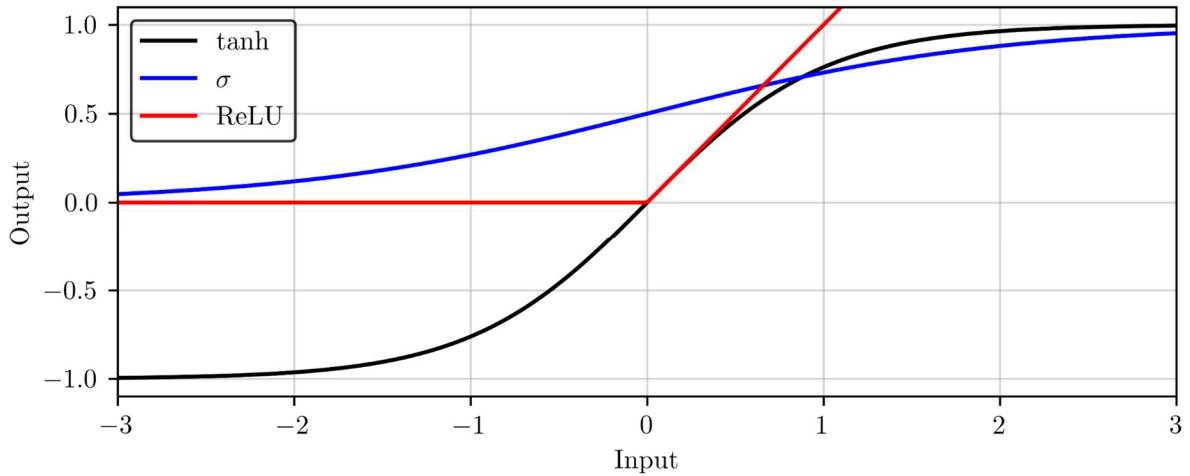


Fig. 4 Activation function comparison. The black plot illustrates the tanh activation function (eq. (46)), the blue plot the sigmoid-function (eq. (43)) and the red plot the ReLU function (eq. (47)).

Even though sigmoid and tanh-functions mimic brain activity more accurately, they suffer from the vanishing gradient problem, where gradients become extremely small during backpropagation, hindering learning in deep networks.⁶⁹ ReLU type activations have gained popularity due to their simplicity and computational efficiency.³¹ ReLU addresses the vanishing gradient problem by avoiding saturation for positive inputs,⁷⁰ accelerating the convergence of gradient-based optimization. However, a ReLU activation function also has its limitations, such as the dying ReLU problem, where neurons output zero and stop learning due to being stuck in the negative side of the function.⁶⁹

Training of ANNs happens with a process called gradient descent, adjusting the biases and weights of each layer. This process involves calculating the gradient with respect to an “error” or loss with a predefined loss function and going from the output back toward the input. The loss function is minimized by adjusting the biases and weights, a process called backpropagation. This method is often extended by various improvements to get toward a local minimum more quickly or to “jump” shallow local minima. More details about these methods can be found in [71].

Multilayer ANNs trained with backpropagation can effectively learn complex patterns and relationships within data.⁷² The more hidden layers inside an ANN, the better it becomes at extracting higher-level features leading to the “Deep Learning” subcategory.⁷³

In conclusion, the selection of activation functions in ANNs is a critical decision that influences the network’s expressive power, approximation capabilities, and overall

performance. Researchers continue to explore and develop novel activation functions to enhance the efficiency of ML models.

5 Methods

The methodologies employed in this research are crucial for obtaining accurate and reliable results. The following sections provide a detailed account of the numerical methods and analytical approaches used. The numerical techniques (5.1) for solving the LLG and obtaining a realistic current distribution are applied from other publications.^{19,32} Also, the method for measuring the drift angle due to an edge as accurately as possible (5.1.3) is a collection of known numerical methods.^{74,75} To the best of my knowledge, the analytical method (5.2) has not yet been presented.

The source code for the numerical methods and the plots for all of the relevant figures can be found in my GitHub repository.⁷⁶

5.1 Numerical Techniques

A range of numerical techniques was applied to solve the complex equations central to this study. These methods ensure precise simulations of various phenomena evolving around magnetism on the microscopic scale. To utilize a GPU's parallelization capabilities, we implemented the iteration algorithms shown in 5.1.1 and 5.1.2 using the PyCUDA library.

5.1.1. Methods for solving the Landau-Lifshitz-Gilbert equation

The LLG equation is essential for understanding magnetization dynamics on a microscale and can be challenging to solve numerically. This subsection explains the basics of the numerical algorithm utilized to obtain the change in the direction of each atomic spin \vec{n} over time with the LLG equation. A particular emphasis is placed on the methods' speed while retaining a stable simulation.

The inherent complexity of the LLG equation presents significant challenges. Since it consists of multiple coupled ordinary differential equations, analytical solutions do not always exist. Only for very limiting cases, like the soliton solution, does an analytical solution exist.^{77,78} The nonlinear nature of the equation, combined with the presence of both precessional and damping terms, further complicates any solutions.

We explored three different methods of numerically integrating the explicit LLG: Euler, Heun, and Runge-Kutta (RK4).

For all methods, it is easier to illustrate their iterative functionality by expressing the right-hand side of the explicit LLG shown in eq. (28) as the “LLG-function” of \vec{n} :

$$\partial_t \vec{n} = \text{LLG}(\vec{n}). \quad (48)$$

$\text{LLG}(\vec{n})$ is hereby calculated with the \vec{H}_{eff} shown in eq. (24). The Euler method is the by far easiest, simply assuming a time step Δt and iterating with:

$$\vec{n}_{t+1} = \vec{n}_t + \Delta t \cdot \text{LLG}(\vec{n}_t) = f_{\text{E}}(\vec{n}_t). \quad (49)$$

Despite its simplicity, it suffers from numerical instability with an error $\mathcal{O}((\Delta t)^2)$. The Heun method makes use of the tangent on the right side of Δt as well, calculating the subsequent orientation of spin \vec{n} in two stages:

$$\vec{n}_{t+1} = \vec{n}_t + (\text{LLG}(\vec{n}_t) + \text{LLG}[f_{\text{E}}(\vec{n}_t)]) \cdot \frac{\Delta t}{2} = f_{\text{H}}(\vec{n}_t). \quad (50)$$

When using the Heun method, GPU memory usage doubles as the first tangent $\text{LLG}(\vec{n}_t)$ needs to be kept in memory during the computation of the second tangent $\text{LLG}[f_{\text{E}}(\vec{n}_t)]$. The error is lower at $\mathcal{O}((\Delta t)^3)$, leading to a 5x greater maximum time step in our simulations compared to Euler’s method. This possibility to do bigger time steps makes Heun’s method computationally more efficient for our system, even considering its higher memory usage.

RK4, which is most often the default for micromagnetic frameworks⁷⁹ utilizes four different tangents (k_1, k_2, k_3, k_4) with:

$$\vec{n}_{t+1} = \vec{n}_t + (k_1 + 2 \cdot k_2 + 2 \cdot k_3 + k_4) \cdot \frac{\Delta t}{2} = f_{\text{RK4}}(\vec{n}_t), \quad (51)$$

and the tangents being defined by:

$$k_1 = \text{LLG}(\vec{n}_t), \quad (52)$$

$$k_2 = \text{LLG}\left(\vec{n}_t + \frac{\Delta t \cdot k_1}{2}\right), \quad (53)$$

$$k_3 = \text{LLG}\left(\vec{n}_t + \frac{\Delta t \cdot k_2}{2}\right), \quad (54)$$

$$k_4 = \text{LLG}(\vec{n}_t + \Delta t \cdot k_3). \quad (55)$$

It features a comparatively low error of $\mathcal{O}((\Delta t)^5)$, but necessitates the usage of 4x more GPU memory.⁷⁸ Even though RK4 allows time steps almost 3x as long as Δt for Heun's method, the runtime on our PHYSnet afs-cluster (2x GTX 2080ti) was slightly higher compared to Heun's method.

For the reasons mentioned above, we utilized Heun's method with $\Delta t = 1.8 \cdot 10^{-14}$ s.

5.1.2. Methods of solving for a realistic current distribution

Determining a realistic current distribution is critical to accurately simulating micromagnetic states influenced by STT. This chapter describes the techniques used to model current flow, considering geometrical constraints. The method presented was introduced to skyrmionic racetracks by Strobel¹⁹ and adapted by us to fit a hexagonal lattice, with the aim of calculating the local current \vec{v}_s every atomic spin is exposed to.¹ The Laplace equation is solved numerically with the finite-difference method and Neumann boundary conditions (NBC) to obtain the electrical potential for each local atomic spin-site. These conditions state that the current cannot exit the racetrack, except at input and output. The finite-difference method can be used as a relaxation technique and only works with a decent approximation of ϕ .

We start the relaxation procedure with the potential for a constant x-current, r_x being the x-coordinate of the respective atom:

$$\phi_0 = |\vec{j}_{\text{in}}| \cdot r_x. \quad (56)$$

Assuming the source to be on the left side and the drain to be on the right side of the racetrack, we iterate with NBC by setting the electrical potential gradient at input/output to,

$$\phi_{\text{in}} = \phi_{\text{in+1}} + |\vec{j}_{\text{in}}| \quad \text{and} \quad \phi_{\text{out}} = \phi_{\text{out+1}} + |\vec{j}_{\text{in}}|, \quad (57)$$

at each step of the relaxation. From the Laplace equation, one can derive the approximation,

¹ \vec{v}_s and \vec{j}_c can be interconverted using eq. (10). A typical value for the polarization p is hereby 0.4.^{6,21,97}

$$\phi \approx \overline{\phi}_{\text{NN}}, \quad (58)$$

using a Taylor series for ϕ_{NN} (s. appendix 11.3). We can replace the missing nearest neighbors of edge atoms. The easiest method we found is to sum up all vectors pointing from the lattice site with missing neighbors to existing neighbors and replace the missing neighbors with the closest neighbor that the vector points toward. This ansatz incorporates NBC as the derivative of ϕ and therefore the current is zero toward the borders (Ohm's law eq. (35)).

This replacement works for most geometries, except for very narrow paths consisting of two or fewer atoms next to each other due to the second neighbors being needed for the replacement potentials there. Considering that we have wider racetracks this limitation is irrelevant for us.

To reach the equilibrium described in eq. (41) faster, we introduce the relaxation parameter ω between 1 and 2, making use of the successive overrelaxation method:¹⁹

$$\phi^{t+1} = (1 - \omega) \cdot \phi^t + \omega \cdot \overline{\phi_{\text{NN}}^t}. \quad (59)$$

After calculating the current distribution with Ohm's law (eq. (35)), the boundary conditions mentioned above are enforced. For a boundary that is neither input nor output, we project the derived current onto the local boundary direction. For an input or output boundary, the current is directly defined via the input current.

The files “current_calculation.py” and “cc_kernel.c” inside my GitHub repository⁷⁶ show our implementation of the described procedure.

5.1.3. Method for exact measurement of drift angles

This chapter explains our method to determine the current that keeps the skyrmion stationary at distance Δ from the edge. From each φ_s we can then obtain the local angle of edge repulsion $\theta_{\vec{F}}$. The angle of edge repulsion $\theta_{\vec{F}}$ is defined by:

$$\theta_{\vec{F}} = \pi - (\varphi_s + \theta_{\text{SkH}}). \quad (60)$$

$\varphi_s + \theta_{\text{SkH}}$ describes the drift direction of the skyrmion as a sum of the current's angle relative to the edge φ_s and the skyrmion Hall angle θ_{SkH} . From Fig. 5, we can obtain $\theta_{\text{SkH}} \approx 0$ for $\beta = \alpha$, as θ_{SkH} is more than two orders of magnitude smaller than φ_s .¹⁹ Therefore, in our simulation, \vec{v}_s directly opposes $\vec{\nu}_{\vec{F}}$.

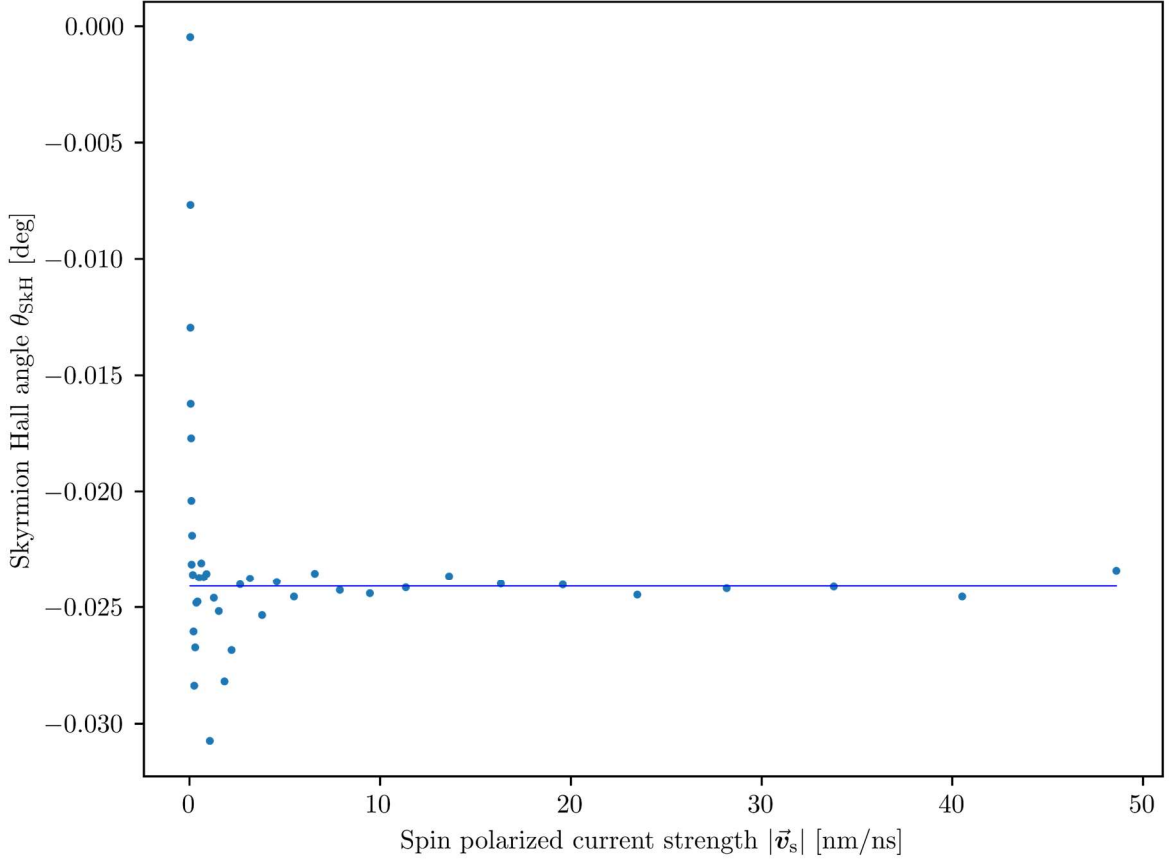


Fig. 5 Plot of θ_{SkH} against $|\vec{v}_s|$. The fit is obtained by fitting all data points with $|\vec{v}_s| > 5 \text{ m/s}$. Below the skyrmions move too little (seen in Fig. 20) to determine the drift angle accurately. Fitting a constant, we obtained $\theta_{\text{SkH}} = 0.024^\circ$ for $\beta = \alpha$.

During the simulation, we track the skyrmion's position and calculate how far it moves from its origin due to a specific current during a particular time δt . As $|\vec{\nu}_{\text{STT}}|/|\vec{v}_s| = a = 0.736$ (s. appendix 11.1) we can directly obtain the current change $\Delta \vec{v}_s$ that counters the induced edge drift $\vec{\nu}_{\vec{F}}$ via,

$$\Delta \vec{v}_s = -\frac{\vec{\nu}_{\text{STT}}}{a} = -\frac{\vec{d}}{\delta t \cdot a}, \quad (61)$$

with the displacement \vec{d} of the skyrmion during δt . A feedback loop then corrects the current iteratively to nullify the drift $\vec{\nu}_{\vec{F}}$, changing the current with a factor called learning rate (l) toward the current that would have kept the skyrmion still. A learning rate of 1 translates to the entire skyrmion displacement being adjusted for with the new current:

$$\vec{v}_{s,t} = \vec{v}_{s,t-1} - \frac{\vec{d} \cdot l}{\delta t \cdot a}. \quad (62)$$

The variable learning rate we found best fit by trial and error was a triangular cyclical change in range $l = [0.1, 1.1]$ with period $T = 10$:

$$l(t) = \left(\frac{l_{\max} - l_{\min}}{\pi} \cdot \arcsin \left(\sin \left(\frac{2\pi}{T} \cdot t \right) \right) + \frac{l_{\max} + l_{\min}}{2} \right) / \delta t. \quad (63)$$

This idea was proposed by Smith et al. in 2017,⁷⁴ enabling a decent rate of change while avoiding an overshooting of the optimal current. We combined this method with reducing the learning rate to its minimum if the drift was inside the defined error range. The combination with this ansatz allows us to adjust the drift velocity after a current has been applied to below $3.3 \cdot 10^{-3}$ m/s for the upper range of the plot (above $4.5 \cdot r_{\text{skyrmion}}$) and below $8.44 \cdot 10^{-4}$ m/s for the lower range of the plot.

The already relaxed skyrmion still relaxes slightly more when placed in a new environment. Therefore, the skyrmion is not placed again for each attempt, but the starting position is the spin configuration with the smallest distance of the skyrmion from the set position after δt . I.e., when a $\vec{v}_{s,t}$ is found that places the skyrmion closer to the starting position, the new spin configuration is chosen for future starting positions.

Considering this initial movement, the optimal current to keep the skyrmion stationary for a certain Δ is found in two different stages. For the first stage, the magnetic configuration is reset after each iteration. For the second stage, the magnetic configuration is not reset after each δt , and \vec{d} is now the movement from the last position instead of the positional vector from the set position. The result can be seen in Fig. 10, showing that $\theta_{\vec{F}}$ stays roughly consistent between 82 and 83 °.

The Python code implementing this functionality can be found in [76] inside the main file, “skyrmion_simulation.py” in the function “simulate” after a check for “spin.v_s_positioning”.

5.2 Analysis with Thiele-type equation

The Thiele ansatz (chapter 4.3.3) offers valuable insights for analyzing skyrmion dynamics. This chapter introduces a method to relate the skyrmion drift direction with an

applied force to the material parameter D . We will define the drift direction due to a force as $\theta_{\vec{F}}$:

$$\theta_{\vec{F}} \stackrel{\vec{v}_s=0}{=} \tan^{-1} \left(\frac{|\vec{\nu}_{\perp \vec{F}}|}{|\vec{\nu}_{\parallel \vec{F}}|} \right) \stackrel{\vec{F}=0}{=} \theta_{\text{SkH}} . \quad (64)$$

Analogous to the skyrmion Hall angle θ_{SkH} and its relation to $\vec{\nu}$ without any force, $\theta_{\vec{F}}$ is the angle between the actual drift direction and the direction of the driving force when no current is applied. For θ_{SkH} the direction of the driving force is given by \vec{v}_s , whereas for $\theta_{\vec{F}}$ it is given by \vec{F} . Splitting the drift into perpendicular and collinear components due to either a force or \vec{v}_s is useful in the context of eq. (34). It allows us to relate different parts of eq. (34) to $\theta_{\vec{F}}$ and θ_{SkH} , as seen in Fig. 6.

$$\vec{\nu} = \frac{1}{G^2 + \alpha^2 D^2} \cdot \left\{ \underbrace{+ (G^2 + \alpha \beta D^2) \cdot \vec{v}_s}_{\vec{\nu}_{\text{ad}}} - \underbrace{D(\beta - \alpha) \cdot \vec{G} \times \vec{v}_s}_{\vec{\nu}_{\text{SkH}}} \underbrace{- \alpha D \vec{F} + \vec{G} \times \vec{F}}_{\vec{\nu}_{\parallel \vec{F}}} \underbrace{\vec{\nu}_{\perp \vec{F}}}_{\vec{\nu}_{\perp \vec{F}}} \right\} \underbrace{\vec{\nu}_{\text{STT}}}_{\vec{\nu}_{\text{STT}}}$$

Fig. 6 Dividing eq. (34) into different drift components for analysis: the drift due to STT $\vec{\nu}_{\text{STT}}$, consisting of an adiabatic component $\vec{\nu}_{\text{ad}}$ and a non-adiabatic component $\vec{\nu}_{\text{SkH}}$ as well as the drift due to a force $\vec{\nu}_{\vec{F}}$, consisting of a component collinear to the force $\vec{\nu}_{\parallel \vec{F}}$ and one perpendicular to the force $\vec{\nu}_{\perp \vec{F}}$.

Separating (64) into two different equations, we split up the drift due to the force $\vec{\nu}_{\vec{F}}$ into the parallel/perpendicular (adiabatic/non-adiabatic) components to this force as $\vec{\nu}_{\perp \vec{F}}$ and $\vec{\nu}_{\parallel \vec{F}}$ respectively:

$$\theta_{\vec{F}} \stackrel{\vec{v}_s=0}{=} \tan^{-1} \left(\frac{|\vec{\nu}_{\perp \vec{F}}|}{|\vec{\nu}_{\parallel \vec{F}}|} \right) ; \quad \tan^{-1} \left(\frac{|\vec{\nu}_{\text{SkH}}|}{|\vec{\nu}_{\text{ad}}|} \right) \stackrel{\vec{F}=0}{=} \theta_{\text{SkH}} . \quad (65)$$

The drift components making up the drift due to a STT $\vec{\nu}_{\text{STT}}$ are named $\vec{\nu}_{\text{ad}}$ and $\vec{\nu}_{\text{SkH}}$. Inserting the respective component for ν_y and ν_x from eq. (34), as illustrated in Fig. 6, we obtain,

$$\theta_{\vec{F}} = \tan^{-1} \left(\frac{-G}{\alpha D} \right), \quad (66)$$

and:

$$\theta_{\text{SkH}} = \tan^{-1} \left(\frac{DG(\alpha - \beta)}{G^2 + \alpha\beta D^2} \right) \quad (67)$$

6 Relevant Assumptions

6.1 Simulation Parameters

The parameters used for our simulations are based on the thin film structure seen in Fig. 7.

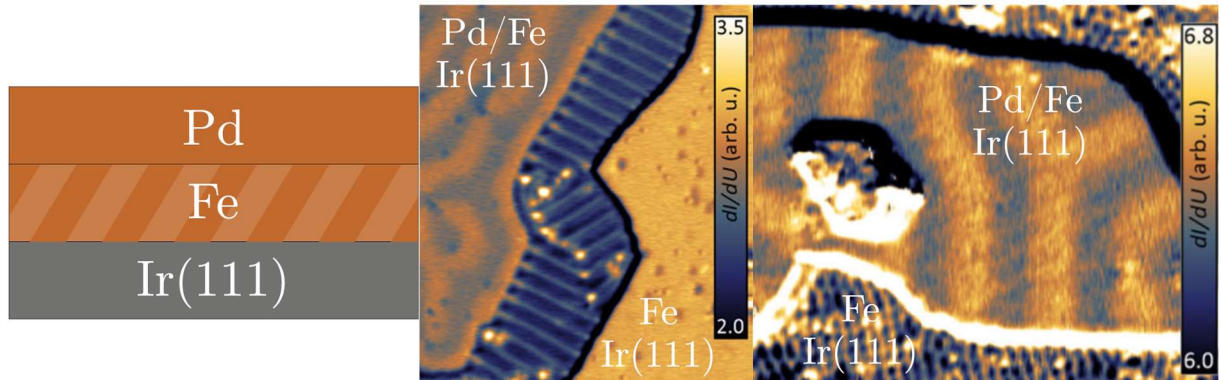


Fig. 7 Layered structure of Pd/Fe bilayer system deposited on Ir(111). In **a**) a sketch of this structure can be seen. **b**) shows some experimental images of this material taken by Spethman et al. [80] with a STM ($\partial I / \partial U$ -maps).

This structure was first experimentally deemed relevant for skyrmionic observations and compressed into effective micromagnetic constants for a single layer by Romming et al.⁸¹

These constants were converted to the relevant parameters for the LLG equation (Tab. 1) with the formulas provided by Hagemeyer et al.⁸² The value for the spin's magnetic moments of $\mu_s = 3 \cdot \mu_b$ was found by Dupé et al.⁸³ and was used throughout the entire simulated area. The height of the Fe-layer is assumed to be $h \approx 4 \text{ \AA}$.⁸⁴

Another assumption is that we look at the atomic spins classically, not quantum mechanically, and that a hexagonal lattice structure with 6 NN is an accurate representation of the Pd/Fe on Ir(111) thin film.

Tab. 1 Standard interaction constants and current parameters for our atomistic simulations if not specified differently. These parameters are used inside the extended LLG equation (eq. (28)). The interaction energies include the material-specific constants J , \vec{D} and k_u . The other relevant parameters include α , β , γ , Δt and μ_s .

Interaction Energies	Other Parameters
$J = 5.78 \text{ meV}$	$\alpha = 0.1$
$D = 1.52 \text{ meV}$	$\beta = \alpha/2, \alpha, \alpha \cdot 2$
$k_u = 0.395 \text{ meV}$	$\gamma = 176.1 \frac{\text{GHz}}{\text{T}}$
$B_z = 1.5 \text{ T} \cdot \mu_s = 0.26 \text{ meV}$	$\Delta t = 1.8 \text{ fs}$
	$\mu_s = 3 \cdot \mu_b$

The DMI-vectors \vec{D} that were used in the LLG can be obtained from D (in Tab. 1) by rotating the vector pointing toward the respective NN (\vec{e}_{NN}) clockwise by $\pi/2$ around the z-axis:

$$\vec{D} = D \cdot \begin{pmatrix} 0 & 1 & 0 \\ -1 & 0 & 0 \\ 0 & 0 & 1 \end{pmatrix} \cdot \vec{e}_{\text{NN}}. \quad (68)$$

We also simulate with $T = 0 \text{ K}$ and therefore have no thermal spin precession or lattice movement. Moreover, we assume the small difference between the atomic radii and, therefore, the resulting lattice mismatch between Pd, Fe, and Ir to be captured by the experimentally determined micromagnetic constants. The anisotropy and demagnetization field is hereby simplified as an easy axis anisotropy.⁸¹

Fluctuations of local μ_s are neglected, and we assume to have a material free of imperfections. The neglected imperfections are most likely the most drastic assumption, as lattice imperfections typically increase close to interfaces. Defects have been shown to change skyrmion dynamics drastically. They could lead to skyrmion annihilation or other effects close to the edge that suppress the repulsion effect found in this work.¹⁹

Moreover, we assume our sample has no electric resistance when calculating a current distribution. Furthermore, the drift due to the spin-Hall effect inducing a spin-current from the Pd layer into the Fe layer is neglected as we assume only to contact the Fe layer directly.

6.2 Analysis

For our analysis, no additional assumptions need to be made to obtain the same qualitative results, except that the LLG is a viable method for simulating local changes in the

magnetic structure in thin films. Our only quantitative assumption is that the Thiele method is reliable for distances bigger than $\Delta \gtrsim 5 \text{ nm} \approx 3.6 r_{\text{Sk}}$ between the skyrmion's center and the simulated edge. If this distance were to change drastically, though, the results would remain the same qualitatively.

7 Results

Many papers have developed methods to avoid any Magnus force affecting the current-driven skyrmionic drift in recent years.^{20–23} In contrast to previous studies, we propose a theoretical concept utilizing this force for advanced computational elements (e.g., a ReLU function). For this purpose, we analyze the skyrmionic edge repulsion in detail, as it includes a strong Magnus force component.

Firstly, in chapter 7.1 the focus is on the creation and relaxation of skyrmions. These can subsequently be placed at specific locations for further simulations. Afterward, a phenomenon is analyzed, which was observed during the testing of our simulations: skyrmions are repelled at an angle from the racetrack's edges without any applied current. In chapter 7.3 principles for later racetrack design are established. Moreover, the impact of the non-perpendicular edge repulsion on realistic current distributions is discussed in the context of different β/α -ratios. Chapter 7.4 combines the results of previous chapters into a racetrack design that features a ReLU output with an adjustable skyrmion bias by varying B_{ext} .

All simulations of atomic magnetic moments are conducted by iterating over the LLG-equation with the method described in chapter 5.1.1. We simulate a hexagonal lattice structure with six nearest neighbors to obtain the magnetic structure of each specific sample over time. The default parameters are listed in Tab. 1 (chapter 6.1). All the Python and C scripts used for this master thesis can be found in [76].

7.1 Skyrmion creation

We take an artificially generated small bubble domain as an initial configuration and start the LLG simulation until equilibrium energy is reached. This preliminary simulation aims to determine the magnetic configuration for a relaxed skyrmion and the energy of a single skyrmion. Various intermediate structures develop during this process, as illustrated in Fig. 8.

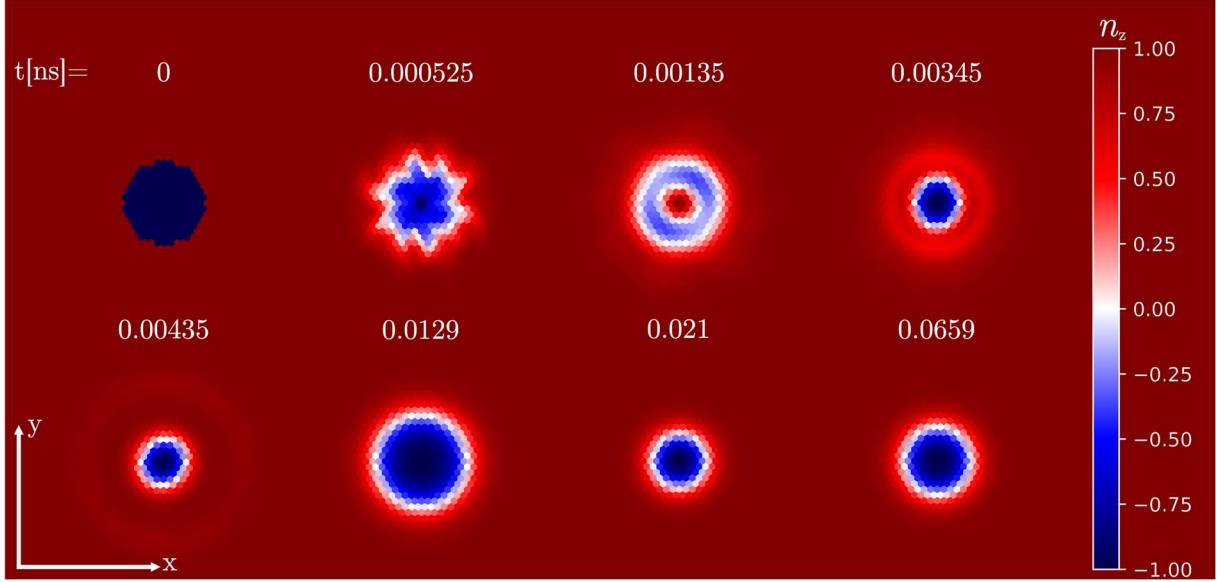


Fig. 8 The z-components of a magnetic texture and their development over time after the spins have been set to the position seen at $t=0$. The time t in ns is written above each structure. Each blue/red/white hexagon depicts the Wigner-Seitz cell for an individual Fe atom, with its color representing the z-component of the respective atomic spin.

The default parameters described in Tab. 1 (chapter 6.1) were also used for this simulation. Time steps were calculated with the method described in chapter 5.1.1, iterating over the LLG with the Heun method. Each time an interaction parameter is modified in the following simulations, this relaxation process is repeated, inserting a relaxed skyrmion into subsequent simulations.

The electric current was dynamically adjusted to gently push the structure toward the center of the simulated area. The skyrmion's location is determined using a center-of-mass approach. To measure the skyrmion's radius r_{Sk} and wall width w_{Sk} , the magnetization's z-components relative to that skyrmion's center were fitted with eq. (19). The simulation concludes when the most significant variance of any spin's z-component inside the simulated area remains below $1 \cdot 10^{-6}$ over a duration of 0.01 ns.

In Fig. 8 the initially created bubble domain transforms into a stable skyrmion, balancing the interaction energies described in chapter 4.1. Initially, there is no wall width between the bubble domain and the surrounding region, rendering the spins at the boundary energetically unfavorable. The typically symmetric shape briefly distorts as the wall width expands rapidly. The spins surpass the equilibrium wall width and initially form a slightly more stable, roughly circular shape at $t = 0.00135$ ns. Temporarily, the skyrmion's core aligns with the external B-field. However, the inverted core collapses quickly

(at $t = 0.003$ ns), resulting in a damped breathing skyrmion mode. By $t = 0.0659$ ns the skyrmion has reached its equilibrium configuration with a w_{Sk} of 0.696 nm and a r_{Sk} of 1.38 nm.

This simulation does not aim to represent an actual implementation inside a potential skyrmionic computational device but illustrates how an equilibrium skyrmionic state can easily be achieved in simulations.

7.2 Skyrmion edge repulsion

Understanding the skyrmion-edge interaction is crucial for gaining more insights into the behavior and stability of skyrmions within racetracks. This chapter focuses on these intrinsic repulsive forces exerted by the boundaries or edges of a racetrack on the skyrmion. We will present a detailed analysis of these repulsive forces and their implications for skyrmion dynamics.

7.2.1. Trajectory of skyrmion due to edge without current

When a repulsive force influences a classical particle, we intuitively expect the particle to be accelerated in the direction of this force. For skyrmions, not being a classical particle, the Thiele equation must be examined to predict this so-called drift. The first simulation aims to build an intuitive understanding of a skyrmion's repulsion by the racetrack edges. We place the skyrmion near the left edge of a $100 \text{ nm} \times 100 \text{ nm}$ sample ($\vec{v}_s = 0$). The initial distance between the skyrmion's center and the edge is $\Delta = 1.6 \cdot r_{\text{Sk}}$ at $y_0 = 50 \text{ nm}$.

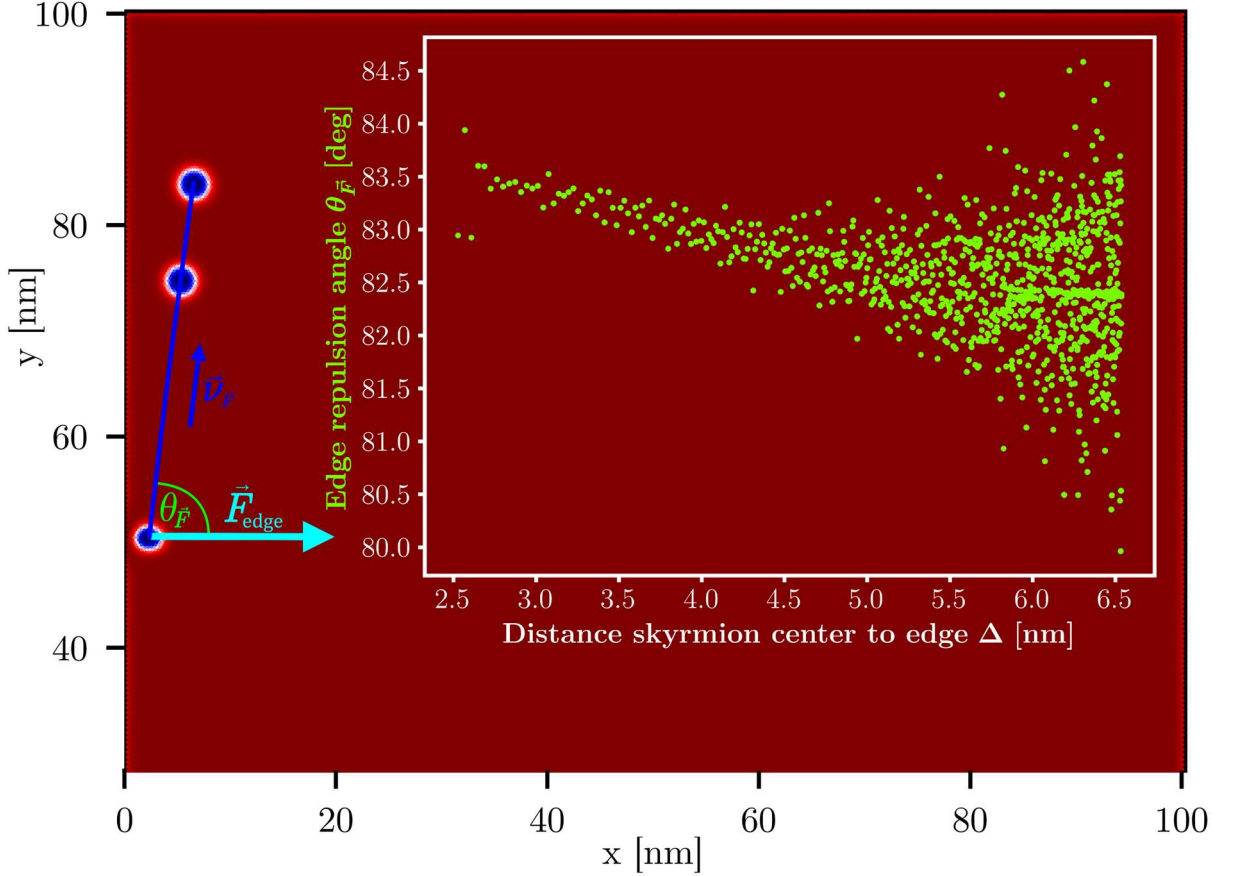


Fig. 9 A skyrmion is created close to a racetrack's edge. The skyrmion's trajectory $\vec{\nu}_F$ is illustrated by the blue line, exemplary skyrmions at $t = [0.01; 2.5; 10]$ ns are shown. The cyan arrow depicts \vec{F}_{edge} . The repulsion angle θ_F is plotted in relation to Δ in the inset graph, considering the angles after $t = 0.05$ ns. The skyrmion's drift significantly deviates from the direction of \vec{F}_{edge} .

From Fig. 9 the resulting skyrmion drift $\vec{\nu}_F$ due to \vec{F}_{edge} can be examined, with the top part of the entire sample being shown. The inset graph plots the skyrmion's edge repulsion angle (θ_F relative to \vec{F}_{edge}) as a function of Δ . From the skyrmion's trajectory, its repulsion angle is derived using central differences of the skyrmion's locations during consecutive time steps.

It can clearly be seen that the drift is far from parallel to \vec{F}_{edge} . The skyrmion drifts at angles in range of $\theta_F = [80, 85]$ ° relative to the force. Being scattered throughout a more extensive range, the relation between θ_F and Δ does not show much continuity. The range of θ_F is this broad due to the skyrmion's shape deforming in an anisotropic manner when a force is introduced, and spin-wave excitations around the skyrmion develop.⁸⁵ This deformation leads to an inaccurate determination of the skyrmion's location with the used center of mass method. During relaxation, the spin waves are absorbed by

Gilbert damping. Waiting until relaxation has finished to obtain the trajectory data is not an option, though, as the skyrmion drifts far enough away from the edge in that time frame to almost nullify \vec{F}_{edge} . Therefore, other methods are introduced to analyze the repulsion in more depth.

7.2.2. Forces on the skyrmion due to an edge.

We create a skyrmion at the distance Δ of $7 \cdot r_{\text{Sk}}$ away from the racetrack's edge and modify a spin polarized current (\vec{v}_s) to keep the skyrmion at the initial position via STT. Afterward, this procedure is repeated for smaller distances. At every distance from the edge \vec{v}_s is adjusted to keep the skyrmion stationary, canceling the skyrmionic drift component due to the edge force ($\vec{\nu}_F$) with a drift component due to STT ($\vec{\nu}_{\text{STT}}$). The method used to determine the parameters for \vec{v}_s and their relation to θ_F are detailed in the chapter 5.1.3.

The output of this simulation is shown in Fig. 10, visualizing the recorded repulsion angles θ_F with respect to the skyrmion's distance from the edge Δ . Additionally, the radius of the skyrmion r_{Sk} as well as the spin polarized current's absolute values $|\vec{v}_s|$ are plotted in the same graph as a function of Δ . Inset is a depiction of the angles from eq. (60) and $\vec{\nu}_F$ counteracting $\vec{\nu}_{\text{STT}}$ at $\Delta = 4 \cdot r_{\text{Sk}}$.

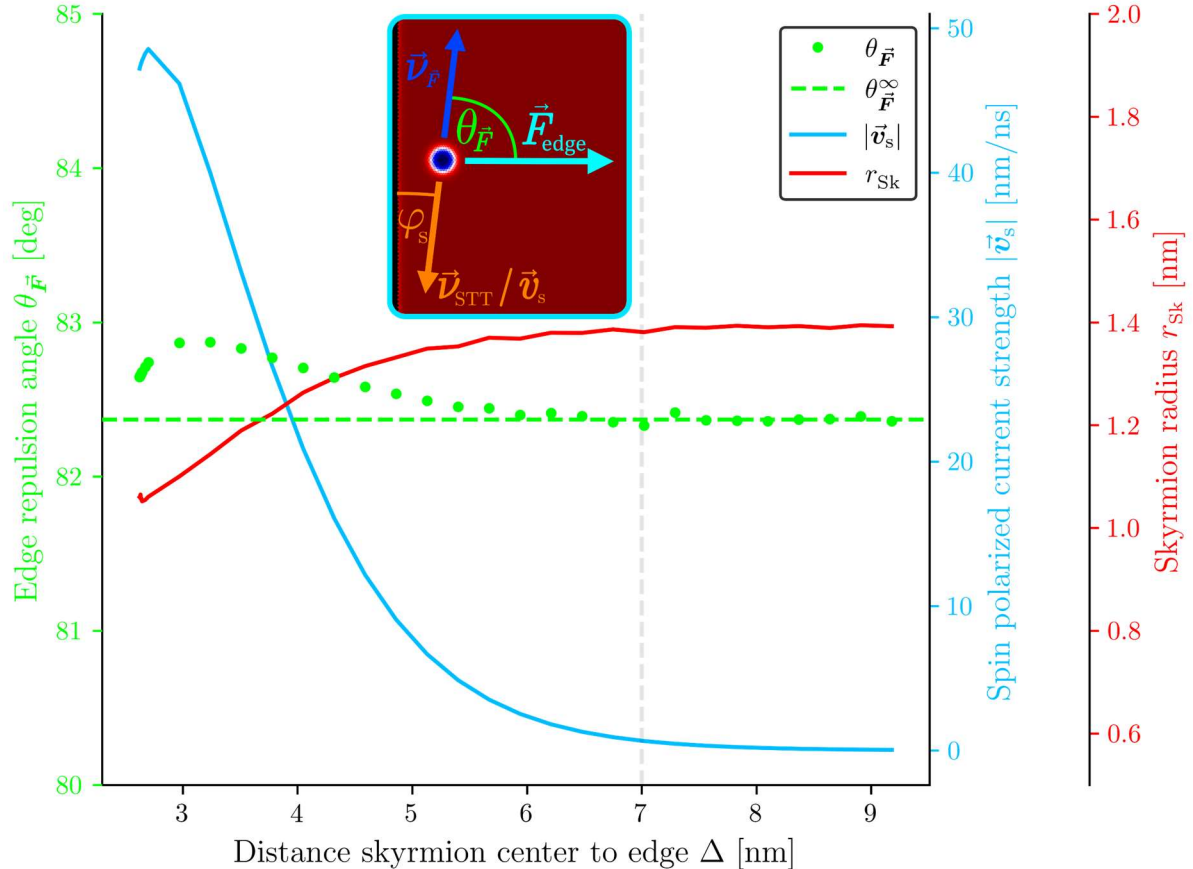


Fig. 10 Compensating for a skyrmion's drift due to an edge with the spin-current \vec{v}_s . The plot shows the development of $\theta_{\vec{F}}$, r_{Sk} and $|\vec{v}_s|$ as a function of Δ , which can be analyzed using a Thiele-type equation. The skyrmion is repelled at different angles depending on its distance from the edge. The inset shows a snapshot from the simulation, illustrating the cancellation of $\vec{\nu}_{\vec{F}}$ with $\vec{\nu}_{STT}$. The inset also depicts the relationship between the corresponding angles $\theta_{\vec{F}}$ and φ_s .

The plot in Fig. 10 can be split into two regimes divided by the gray dashed line at $\Delta \approx 7$ nm.

$\theta_{\vec{F}}^\infty$ describes the repulsion angle for $\Delta > 7$ nm and is almost constant at 82.37° . $|\vec{v}_s|$ is small there and r_{Sk} equals the radius of a relaxed skyrmion not confined by racetrack edges. The trajectory in this regime can be analyzed using the Thiele equation.

For $\Delta > 7$ nm the skyrmion radius r_{Sk} and $\theta_{\vec{F}}$ are not constant anymore. The local repulsion angle increases to a maximum of $\theta_{\vec{F}}^{\max} = 82.87^\circ$ before it drops when Δ gets even smaller. As Thiele assumes a rigid body skyrmion that is not changing in size or shape, the skyrmion deformation invalidates any Thiele-type ansatz in the regime close to the edge. Taking the definition of G from eq. (32) one can directly calculate the eigenvalue of the Diffusion tensor with eq. (66). Inserting $\theta_{\vec{F}}^\infty$ results in $D = -4.213 \cdot 10^{-14}$ kg/s.

Concluding from this chapter, a skyrmion does not drift directly in the direction of an applied force (like \vec{F}_{edge}), but at an angle to it. This behavior has been mentioned in other studies before, but to the best of our knowledge, it has never been studied in any detail without other external driving forces (like a current)⁸⁶. Moreover, the effects of this non-perpendicular edge repulsion on racetrack design are immense, explaining many studies conducted during the last decade.^{20,28–30,87,88}

The edge force affects a skyrmion similarly to any other force acting upon it and induces a drift.^{89,90} We split up this drift due to \vec{F}_{edge} into a collinear and transversal component relative to the acting force ($\vec{\nu}_{\perp\vec{F}}$, $\vec{\nu}_{\parallel\vec{F}}$). The drift component induced solely by an edge and transverse to the edge force we will call edge Magnus drift (EMD) in the following.

7.3 Establishing principles for racetrack design

To utilize the unique skyrmion dynamics in computation devices, this chapter aims to translate those dynamics into general principles for racetrack design. The initial simulations presented in this chapter build upon the knowledge established in the previous chapter, focusing on systems that include a spin polarized current. Chapter 7.3.1

examines the skyrmion's drift due to spin polarized currents with varying β values. Subsequently, in chapter 7.3.2, we analyze the skyrmion's drift when pushed against a racetrack's edge. The final part of this chapter (7.3.3) applies the insights gained to samples with a non-uniform current distribution, establishing principles for the general design of racetracks.

7.3.1. Exploring the trajectory with respect to the β/α relation

Racetracks must combine specific magnetic properties to operate successfully using skyrmions. These include a high spin-orbit coupling, essential for significant DMI strength, and strong perpendicular magnetic anisotropy. Additionally, to function as a suitable racetrack, the β and α values of the material are particularly important as they determine the equilibrium velocity that skyrmions achieve within the racetrack. This section aims to connect β and α with non-perpendicular edge repulsion, leading to different drift velocities inside a racetrack. The conducted simulations are structured as follows: A skyrmion is created at the left side of a rectangular racetrack (Fig. 11) and is driven by a constant current in x-direction ($v_{s,x} = 2.7$ m/s). We look at three different β/α -relations: $\beta = \alpha/2$, $\beta = \alpha$ and $\beta = \alpha \cdot 2$. The other parameters for each sample are the same.

These are typical ratios chosen in many other publications.^{19,28}

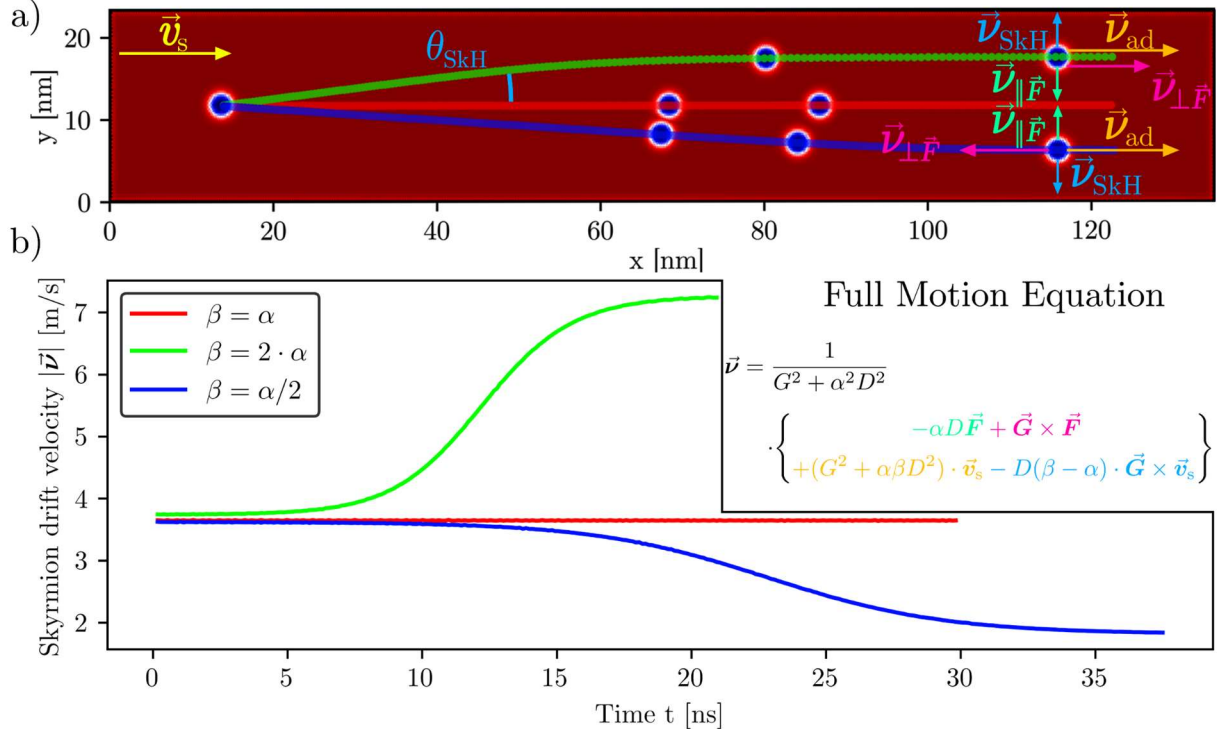


Fig. 11 In a) the skyrmion drift for different ratios of α/β is illustrated. Simulations are conducted with $\beta = \alpha/2$, $\beta = \alpha$, and $\beta = 2\alpha$. The skyrmion paths are colored blue, red, and green, respectively. Skyrmions are shown at $t = [0, 15, 20]$ ns for all different β s and at $t = 33.72$ ns for the low β -value. The

correlated skyrmion drift velocities depending on the ratio of α/β are depicted in **b**). The contribution of each term of the full motion equation to the total drift $\vec{\nu}$ is shown in **a**) with $\vec{\nu}_{\text{ad}}$, $\vec{\nu}_{\text{SkH}}$, $\vec{\nu}_{\parallel \vec{F}}$, and $\vec{\nu}_{\perp \vec{F}}$ colored the same as the respective part of the equation.

After starting the simulation with a skyrmion at $(x_0, y_0) = (14, 11.7)$ nm its drift is initially governed by STT (\vec{v}_s yellow in Fig. 11). The adiabatic part of the STT (orange in Fig. 11) moves the skyrmion collinearly to the spin polarized current with $\vec{\nu}_{\text{ad}}$ toward a positive x-direction. The non-adiabatic part of the STT is quantitatively described by the last term in the drift equation (light blue in Fig. 11). The skyrmion drift that results from non-adiabatic STT is denoted as $\vec{\nu}_{\text{SkH}}$. The vector $\vec{\nu}_{\text{SkH}}$ points toward the positive or negative y-direction, depending on the ratio of β to α as illustrated in eq. (67). Due to a combination of both STT contributions, the skyrmion drifts at an angle of θ_{SkH} relative to the applied current.

In the previous chapter, the diffusion tensor's eigenvalue was calculated with $\theta_{\vec{F}}$, but it can also be calculated with θ_{SkH} . Entering $\theta_{\text{SkH}} = -3.81^\circ$ obtained for $\beta = 0.05$ into eq. (67), yields $D = -4.205 \cdot 10^{-14} \text{ kg/s}$. Using $\theta_{\text{SkH}} = 7.335^\circ$ obtained for $\beta = 0.2$ results in $D = -4.227 \cdot 10^{-14} \text{ kg/s}$ and therefore, an average of $D = -4.216 \cdot 10^{-14} \text{ kg/s}$. This is well within the error range of the given interaction constants in Tab. 1 (chapter 6.1) and confirms the D -value calculated from $\theta_{\vec{F}}$.

When the skyrmion approaches the top or bottom edge of the racetrack, \vec{F}_{edge} reaches a non-negligible strength. The force due to the top edge points downwards, and the force due to the bottom edge points upwards. The skyrmion is redirected toward the interior by edge repulsion $\vec{\nu}_{\vec{F}}$. This edge repulsion can also be split into adiabatic edge repulsion ($\vec{\nu}_{\parallel \vec{F}}$, light green in Fig. 11) and the non-adiabatic edge repulsion or EMD ($\vec{\nu}_{\perp \vec{F}}$, pink in Fig. 11). The adiabatic edge repulsion counteracts $\vec{\nu}_{\text{SkH}}$ more and more until $\nu_y = 0$. Subsequently, the skyrmion proceeds toward the end of the racetrack with a constant $\nu_x = |\vec{\nu}_{\perp \vec{F}} + \vec{\nu}_{\text{ad}}|$. As $\vec{\nu}_{\perp \vec{F}}$ points toward opposite directions when the skyrmion is pushed against the top or bottom edge, ν_x is different for the different β/α -ratios. At the top edge, the EMD accelerates the skyrmion, and at the bottom edge, the EMD decelerates the skyrmion. When an equilibrium between $\vec{\nu}_{\text{SkH}}$ and $\vec{\nu}_{\parallel \vec{F}}$ is reached, the ν_x -values become 1.84 m/s for $\beta = \alpha/2$, 3.65 m/s for $\beta = \alpha$ and 7.24 m/s for $\beta = 2\alpha$, as seen in Fig. 11 **b**). These ν_x are reached after $t \approx 38$ ns for $\beta = \alpha/2$, $t \approx 30$ ns for $\beta = \alpha$ and $t \approx 22$ ns for $\beta = 2\alpha$.

This drift speed variation for different β -values is a well-known phenomenon, has been predicted in several theoretical studies^{29,30} and confirmed qualitatively in experiments by

Jiang et al. in 2016.²⁷ However, it has never been categorized as an intrinsic edge effect resulting from non-perpendicular edge repulsion and has always been correlated to a spin polarized current.

Drift speed is directly connected to the operational speed (t/N_{Sk}) of a future skyrmionic device. Therefore, the racetrack's efficiency and function are strongly impacted by $\vec{\nu}_{\perp \vec{F}}$, which in turn directly depends on $\vec{\nu}_{SkH}$. Materials with $\beta > \alpha$ should consequently be favored because $\vec{\nu}_{SkH}$ then points toward the top edge for those. This relation will be explored further in the upcoming chapter.

7.3.2. Current influenced skyrmion edge interaction

When designing a more complex racetrack geometry, it is useful to understand how exactly a skyrmion is repelled when pushed into an edge with different velocities and at different angles.

To change the speed and angle of the skyrmion's movement, one could change α and β to different values while keeping NBC and a constant current in x-direction. As the relation between α , β and φ_s is not linear though (s. eq. (34)), we chose to alter $|\vec{v}_s|$ and φ_s directly while keeping $\beta = 0.1$. This approach simplifies maintaining a constant skyrmion drift speed or angle.

In the simulations described in this chapter, we angle the current downwards to investigate the pinning and annihilation thresholds due to interaction with the bottom edge (interaction with top edge will be discussed in chapter 7.4.2). Possible scenarios of simulation outcomes are shown in Fig. 12 a). Three parameters can be varied to achieve different results: the angle φ_s of the applied current relative to the racetrack edge, the strength of the applied current $|\vec{v}_s|$ and the possible addition of a step in an otherwise atomically flat bottom texture (s. zoomed-in area in Fig. 12).

If the bottom edge is atomically flat, there are three possible outcomes of a simulation varying φ_s and $|\vec{v}_s|$:

1. The skyrmion drifts along the edge until it reaches the racetrack's end at $x = 135$ nm.
2. The skyrmion is repelled backward by the edge, finishing at the start of the racetrack at $x = 0$ nm.
3. The skyrmion is annihilated at the edge ($y = 0$) of the track.

When an atomic step at the racetrack's edge is introduced, another result becomes possible:

4. The skyrmion is pinned at the step ($x = 85$ nm)

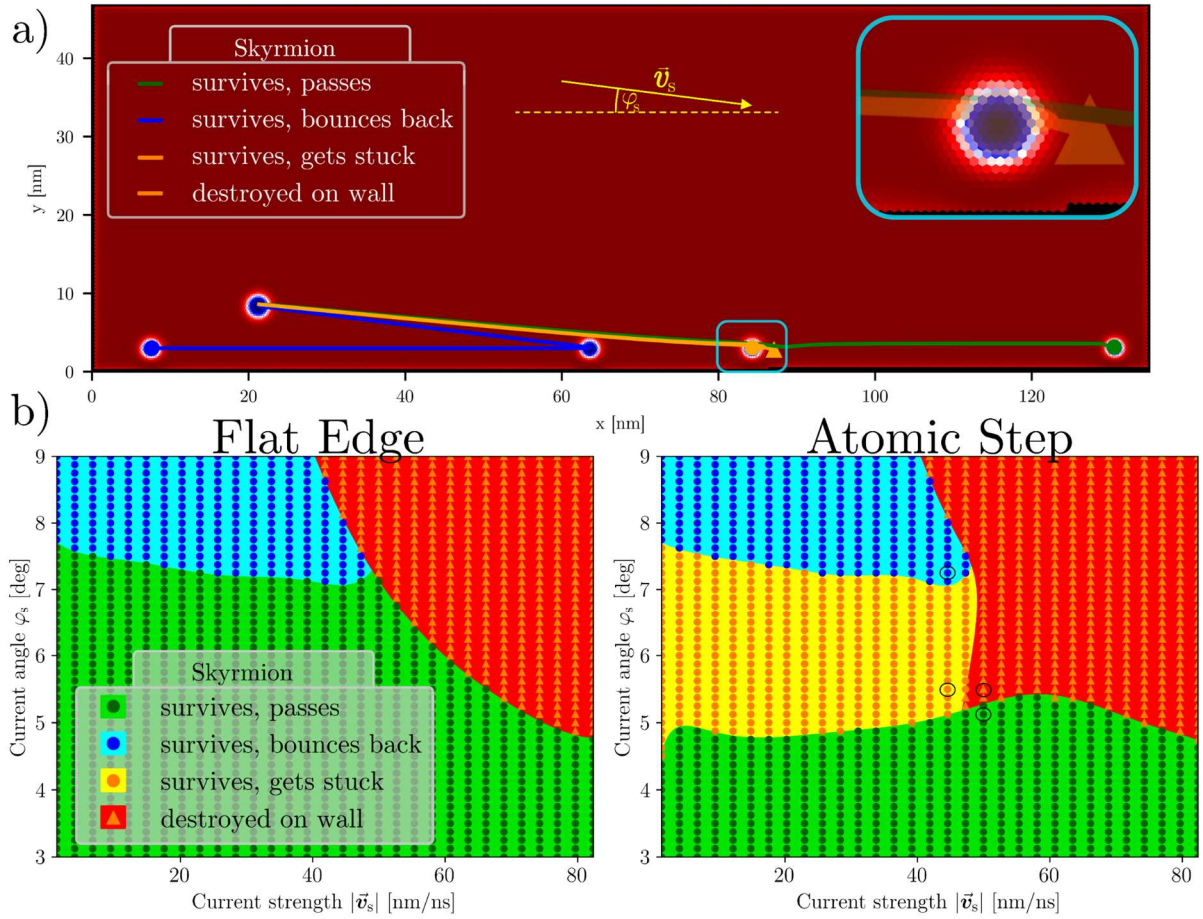


Fig. 12 **a)** shows exemplary trajectories for the four types of results when an atomic step is present at the bottom of a racetrack. The applied current \vec{v}_s is illustrated in yellow. An exemplary skyrmion trajectory is shown for each of the four outcomes described in the legend. Skyrmions are inset at significant locations of each outcome. A zoomed-in area at the top right illustrates the atomic step. **b)** shows phase diagrams comparing simulation outcomes for different $|\vec{v}_s|$ and φ_s . Each small shape represents the outcome of one simulation according to the legend in **a)**. The sample simulated for the outcomes shown in the left diagram is atomically flat at the borders; the one simulated for the right diagram has one atomic step at $x \approx 85$ nm. The black circles in the right diagram mark the parameters for the trajectories shown in **a)**.

When the skyrmion velocity relative to the edge becomes too large, the skyrmion annihilates at the edge of the racetrack (red area in Fig. 12). Skyrmion annihilation has been thoroughly examined in other studies already^{19,20,23}(s. chapter 3.2), but never quantitatively studied throughout a broader range of φ_s or θ_{SkH} . From Fig. 12 **b**), it can be seen that φ_s plays an important role when determining the annihilation threshold $|\vec{v}_s|$. The larger φ_s the smaller $|\vec{v}_s|$ at which the skyrmion is already annihilated. If the edge that the skyrmion is pushed against is not flat but has a bump or tip, the skyrmion is annihilated at a lower $|\vec{v}_s|$. This result coincides with Zhang's⁹¹ findings from 2015.

As the skyrmion is pressed against the edge by the spin polarized current, it must overcome the step to continue drifting with a small enough current to reach the end of the racetrack. The main phenomenon underlying the pinning and passing thresholds in Fig. 12 is the EMD, causing a non-perpendicular edge repulsion. If the edge is flat, the skyrmion passes to the output at a maximum current angle of $\varphi_s^{\max,\text{pass}} = 7.7^\circ$ at the low current limit. As $|\vec{v}_s|$ increases, $\varphi_s^{\max,\text{pass}}$ decreases to 7.0° . The maximum angle at which the skyrmion passes through the racetrack without pinning can be approximated by eq. (60) when using the associated $\theta_{\vec{F}}$ determined in chapter 7.2.2. Introducing an atomic step reduces $\varphi_s^{\max,\text{pass}}$ to 5° as in the range $\varphi_s \approx [5.0, 7.7]^\circ$ the skyrmion is getting pinned at the atomic step. The pinning occurs because r_{Sk} is of the same order of magnitude as a single atomic step and not much greater.

Notably, atomic steps automatically occur if the racetrack is not aligned exactly along one of the 3 symmetry axes of the hexagonal lattice structure. Additionally $\varphi_s^{\max,\text{pass}}$ further decreases with increasing edge roughness¹⁹.

7.3.3. Skyrmion dynamics for realistic current distributions

Following the previous findings, we shift our simulations to realistic current distributions, extending our investigation into the pinning of skyrmions at the edges of a racetrack. The leftmost atoms of the sample are designated as the input, while the rightmost atoms serve as the output. Neumann boundary conditions (NBC) ensure that current cannot exit or enter an edge, except at input and output locations, where the current is defined by $|\vec{v}_{s,\text{in}}|$. Further details regarding the current calculation can be found in chapter 4.4 and 5.1.2.

We will briefly examine the parameters necessary to achieve pinning with NBC on a straight racetrack with an atomic step (s. Fig. 12). To drive the skyrmion toward the edge, a very small β (relative to α) is necessary. On a straight racetrack β must be less than 0.0343 when $\alpha = 0.1$ to successfully pin a skyrmion with the parameters from Tab. 1 (chapter 6.1). This critically small β/α -relation has not been reported so far, to the best of my knowledge (s. 3.2).

Therefore, we modify the simple straight design to achieve dynamic pinning of skyrmions at specific spots of the racetrack. This is possible because currents passing at finite distances from an edge influence the finitely sized skyrmion. Two key geometries allow a skyrmion to be pushed toward an edge by the current, even when $\beta = \alpha$:

1. Sharp corners: sites, where the racetrack's direction changes abruptly
2. Pinch points: sites, where the racetrack's width narrows rapidly

These racetrack features can be modified to induce different behaviors. Fig. 13 and Fig. 14 illustrate examples of pinch points and sharp corners, respectively. The reason for skyrmion pinning at these specific sites is the way current flows around sharp corners or through pinch points compared to smoother sections. This becomes apparent when observing φ_s , the angle of the current relative to the local edge (indicated by a green stripe). Pinning occurs when φ_s , pushing the skyrmion toward the edge, becomes too big (Fig. 13/Fig. 14 sample 2 zoom-in).

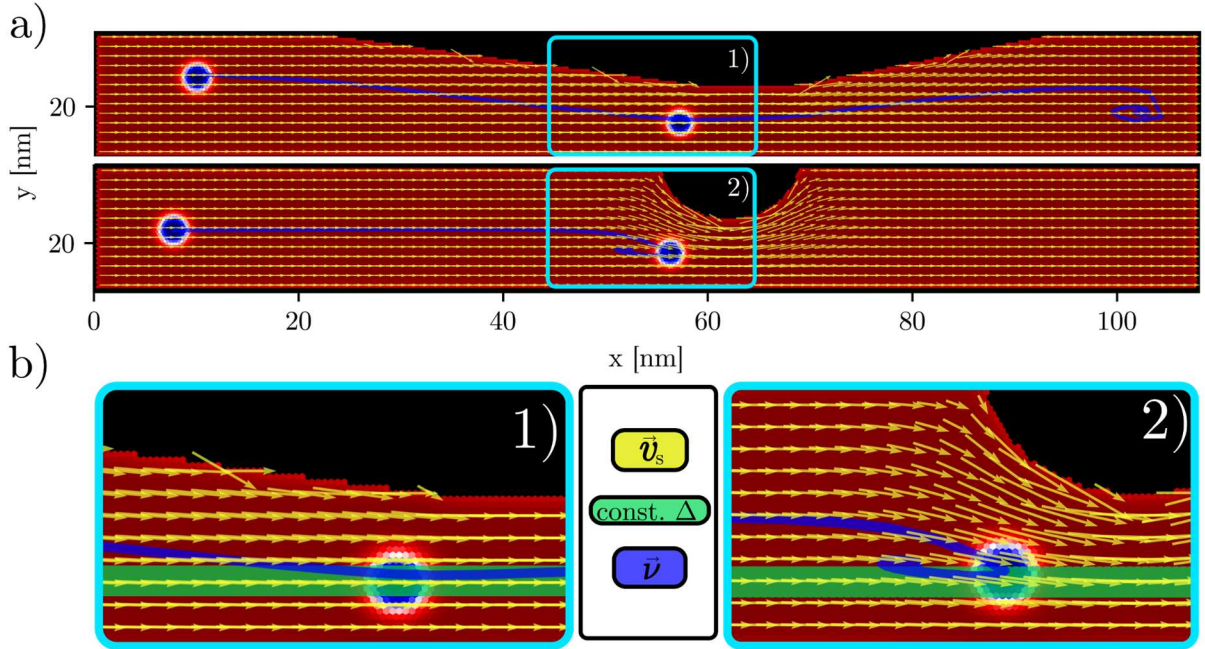


Fig. 13 Two distinct racetracks featuring a pinch point are depicted in **a**). Sample 1) allows the skyrmion to pass toward the output, while sample 2) pins the skyrmion. The yellow arrows denote \vec{v}_s for every fourth atomic site, whereas the skyrmion drift $\vec{\nu}$ at $|\vec{v}_{s,in}| = 2.7$ m/s is illustrated in blue with two skyrmion examples shown. In **b**), a zoomed-in view of both samples is presented. The green stripe maintains a constant distance from the bottom edge. Pinning may occur if a sharp pinch point is present within a racetrack.

Various parameters can be adjusted to achieve either passing or pinning of skyrmions. Even slight modifications to $|\vec{v}_{s,in}|$, α , β , racetrack width and the racetrack's edge geometry can alter the outcome.

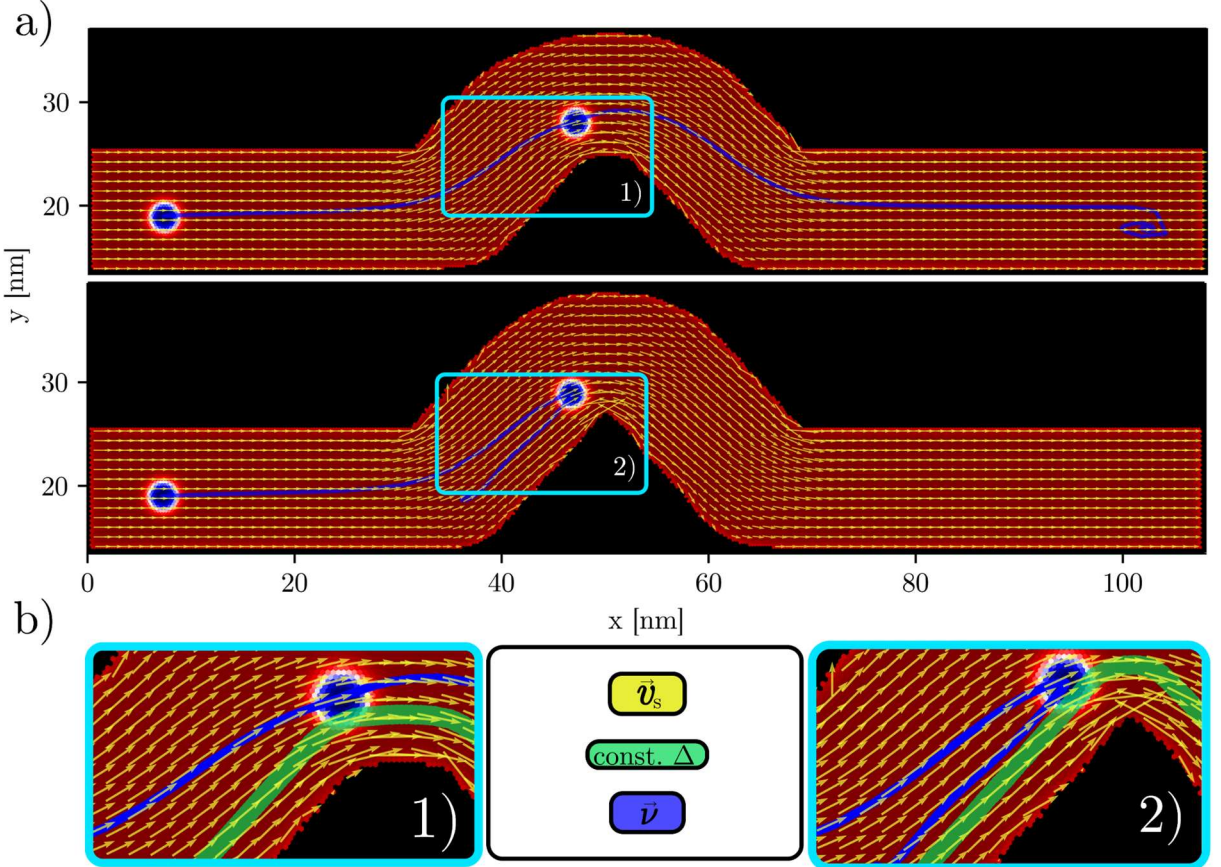


Fig. 14 Two distinct racetracks featuring a corner are depicted in a). Sample 1) allows the skyrmion to pass toward the output, while sample 2) pins the skyrmion. The effect of both mellow and a sharp racetrack corner on the skyrmion trajectory is analyzed analogously to the pinch point analysis shown in Fig. 13. The input current $|\vec{v}_{s,\text{in}}| = 2.7 \text{ m/s}$. If a sharp corner is present within a racetrack, pinning may occur.

Removing or adding a single atom at the tip of a corner can determine whether the skyrmion is pinned.

Summarizing the results from this chapter (Fig. 13 and Fig. 14) and the insights from chapter 7.2, pinning can occur due to four different factors considering a realistic current distribution. All these factors stem from a non-perpendicular edge repulsion, as described by the Thiele equation:

Firstly, the material parameters α and β affect θ_{SkH} , thereby affecting the pinning potential.

Secondly, pinch points influence skyrmions by pushing them against an edge. If this edge happens to be the one that slows the skyrmion down, the skyrmion can be pinned.

Thirdly, sharp corners can also pin skyrmions if the corner changes the racetrack's orientation in such a way that the vector along the axis of the racetrack toward the output becomes more parallel to the vector $\vec{\nu} \times \vec{G}$. Only this specific geometry of the

corner part can pin the skyrmion because then the edge interaction has a component opposing the adiabatic STT induced skyrmion drift.

Fourthly, changing the input current, $|\vec{v}_{s,in}|$ also influences if a skyrmion is pinned. Generally, a stronger current enables skyrmions to overcome a potential pinning site due to corners or pinch points. However, a weaker current does not push the skyrmion that close to the racetrack's edge. As the repulsion angle is slightly bigger when the skyrmion is close to the edge (s. Fig. 10), a weaker current can occasionally result in a slightly bigger $\varphi_s^{\max,\text{pass}}$ (s. Fig. 12). Therefore, pinning is sometimes avoided with a smaller $|\vec{v}_{s,in}|$ for specific racetrack designs and materials.

These four pinning causes are additive, meaning a slight pinch point combined with a few atomic steps and $\beta < \alpha$ can also result in pinning.

The key takeaway for designing racetracks is to monitor possible pinning sites and their intricate properties. During the design process, the strength and interaction of these pinning sites with the skyrmions should be varied strategically to achieve the desired outcome. We aim for simple designs and consistency of the outcome regarding material parameters, input current, and design changes.

7.4 Designing a skyrmion based ReLU racetrack

Even though having been used in neural networks for a long time⁹² ReLU-functions have only recently³¹ become a focus of AI research. In this chapter, we present a skyrmionic racetrack design whose number of skyrmions reaching the output (N_{Sk}^{out}) can be described by the following ReLU function:

$$N_{Sk}^{out} = \max(0, N_{Sk}^{in} - b). \quad (69)$$

For its implementation in ANNs the bias b can be varied by changing B_{ext} . Skyrmions are propelled forward inside the racetrack by an applied in-plane spin polarized current. The local \vec{v}_s is calculated by relaxing the electric potential using the principles and methods described in chapter 4.4 and 5.1.2.

Initially, a racetrack design based on $\beta = \alpha/2$ will be introduced. This design will be modified in chapter 7.4.2 to work with systems where $\beta > \alpha$. The bias of the ReLU function can be adjusted for both β values to some degree by varying the external magnetic field.

7.4.1. Case 1: $\alpha > \beta$

Achieving a non-linear output from a skyrmionic racetrack can be easily accomplished with designs such as the atomic step racetrack from the repulsion test shown in Fig. 12. In this simple design, the atomic step is the pinning site. The second skyrmion pushes the first one, which is pinned beyond the pinning site. Subsequently, the second skyrmion is pinned at this site. This is just one example of a design we tried, but all of them, if even working, are generally limited by their requirement for very small β -values and/or a lack of bias adjustability (in this case $b = 1$).

After a lot of trial and error, we came up with the racetrack design shown in Fig. 15. Its output is scalable to different biases by adjusting B_{ext} , which affects the skyrmions' size. The racetrack consists of a cavity attached to a rectangular racetrack. This cavity is a rounded rectangle with a pathway toward the rectangular racetrack. The pathway features rounded corners toward the main racetrack and sharp corners toward the cavity. Marked with a light blue arrow in Fig. 15 is the “dynamic” pinning site (right rounded corner of the pathway).

Skyrmions are positioned inside the racetrack every 6.67 ns at $(x_0, y_0) = (10.8, 32.7)$ nm and propelled forward by a spin polarized current calculated from NBC. The following figures illustrate skyrmions and/or magnetic configurations at different times after the simulation starts (t).

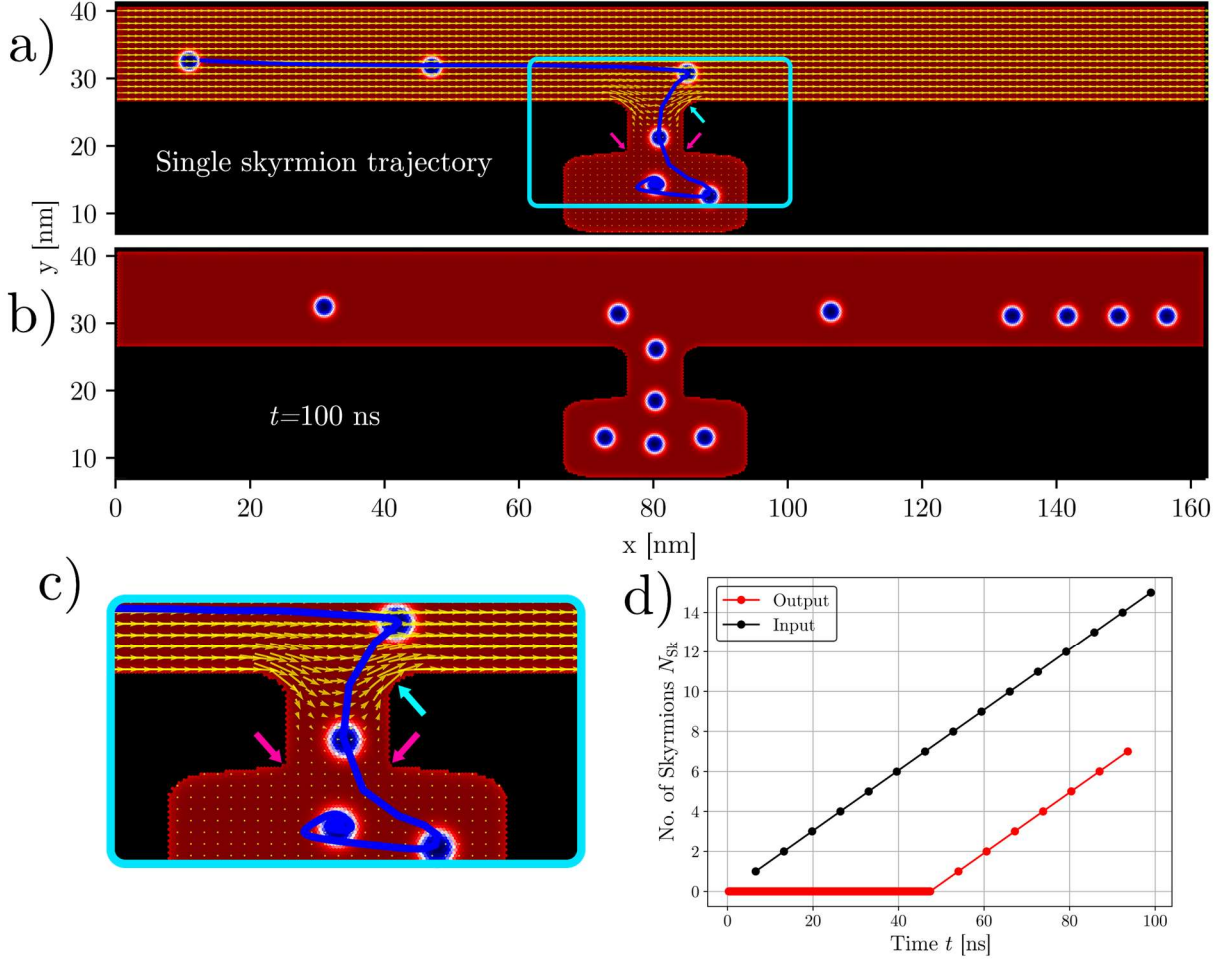


Fig. 15 The ReLU racetrack design for $\beta = \alpha/2$ featuring a cavity. The current distribution is shown in **a**). The trajectory for $|\vec{v}_{s,\text{in}}| = 2.70$ m/s of a single skyrmion drifting into the cavity at $B_{\text{ext}} = 1.5$ T is plotted in blue. The skyrmion is shown at $t = [5, 11, 12, 13, 79]$ ns. The sharp inner corners and the “dynamic” pinning site are marked with pink/light blue arrows, respectively. In **b**), the magnetic configuration at $t = 100$ ns is displayed after skyrmions are introduced every 6.67 ns. In **c**), a zoomed-in area of the cavity’s entrance/exit is presented. In **d**), the number of skyrmions that have entered the racetrack (input) and the number of skyrmions that have reached the racetrack’s output are plotted as a function of t .

Due to $\beta = \alpha/2$ the skyrmion is propelled toward the bottom edge. The “dynamic” pinning site redirects the skyrmions back into the cavity. Subsequent skyrmions either enter the cavity like the first one, move past the cavity toward the output, or become pinned at the entrance to the cavity. This behavior depends on the upward push from skyrmions already inside the cavity, the forward push by trailing skyrmions, as well as $|\vec{v}_{s,\text{in}}|$.

The bias b can be adjusted by varying B_{ext} within a range of [1.1, 2.0] T. It is crucial that the two inward-facing corners of the cavity (highlighted by pink arrows in Fig. 15)

remain relatively sharp. The functional B_{ext} range is this broad only because the sharp inner corners of the connecting pathway limit the upward push of skyrmions within the cavity. For $B_{\text{ext}} = 1.5$ T we found a functional range for $|\vec{v}_{s,\text{in}}|$ of [2.70,5.40] m/s. Above this $|\vec{v}_{s,\text{in}}|$ range, the skyrmions are annihilated at the edge of the connecting pathway; below, they do not enter the cavity.

In theory as B_{ext} increases, the skyrmion size decreases⁹³, necessitating more skyrmions to fill up the cavity and increase the bias. However, simulations show that skyrmions not only fill up the cavity ($N_{\text{Sk}}^{\text{cav}}$), but also aggregate in front of the cavity ($N_{\text{Sk}}^{\text{agg}}$), contributing significantly to the total bias (illustrated in Fig. 16 b)):

$$b = N_{\text{Sk}}^{\text{cav}} + N_{\text{Sk}}^{\text{agg}}. \quad (70)$$

Inside the lower range of B_{ext} (from 1.1 T to 1.5 T), the skyrmion configuration inside the cavity does not change qualitatively. Only the upmost skyrmion inside the connecting pathway between the cavity and the rectangular racetrack sits slightly lower (s. green lines in Fig. 16 as a reference). Thus, $N_{\text{Sk}}^{\text{cav}}$ remains the same, and more importantly, $N_{\text{Sk}}^{\text{agg}}$ decreases with increasing B_{ext} . This phenomenon is illustrated in Fig. 16 a) resulting in the B_{ext} vs. b relationship shown in Fig. 16 c).

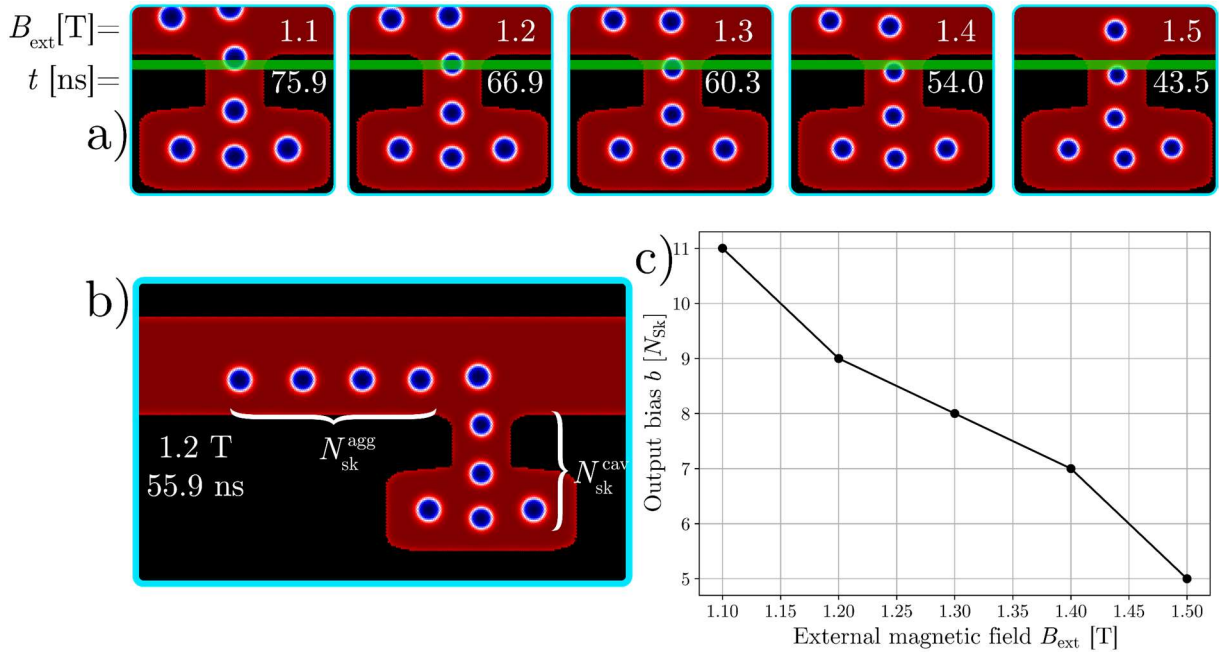


Fig. 16 Analysis of the ReLU behavior from the racetrack presented in Fig. 15. In a), the magnetic configuration (after periodic skyrmion input) is shown around the cavity at $B_{\text{ext}} = [1.1, 1.2, 1.3, 1.4, 1.5]$ T. The current distribution, shown in Fig. 15 a), propels the skyrmions forward via STT with $\beta = \alpha/2$ and $|\vec{v}_{s,\text{in}}| = 2.70$ m/s. The green transparent stripe is at the same position for all samples. In b), a larger

section of an exemplary racetrack from a) is depicted to illustrate $N_{\text{Sk}}^{\text{agg}}$ and $N_{\text{Sk}}^{\text{cav}}$. In c), the bias b is plotted as a function of the external magnetic field B_{ext} . The bias can be modified within the range $b = [11, 5]$ skyrmions.

The curve indicates that adjusting B_{ext} within the range of 1.1 to 1.5 T allows for a roughly continuous modification of the racetrack's output bias from 11 to 5 skyrmions. The output below the lower end of this B_{ext} range does not maintain a strict ReLU shape. Instead, multiple $N_{\text{Sk}}^{\text{agg}}$ are released after an accumulation in front of the cavity.

Beyond the B_{ext} range shown in Fig. 16, up to $B_{\text{ext}} = 2.0$ T, $N_{\text{sk}}^{\text{cav}}$ increases in discrete steps with rising B_{ext} . Interestingly, for the given cavity size and shape, two of those steps occur in the B_{ext} range of [1.6, 2.0] T (Fig. 17). At each discrete step, the magnetic configuration inside the cavity changes qualitatively: once between 1.6 T and 1.7 T, and again between 1.9 T and 2.0 T. Both changes cause jumps in $N_{\text{sk}}^{\text{cav}}$ and consequently in b .

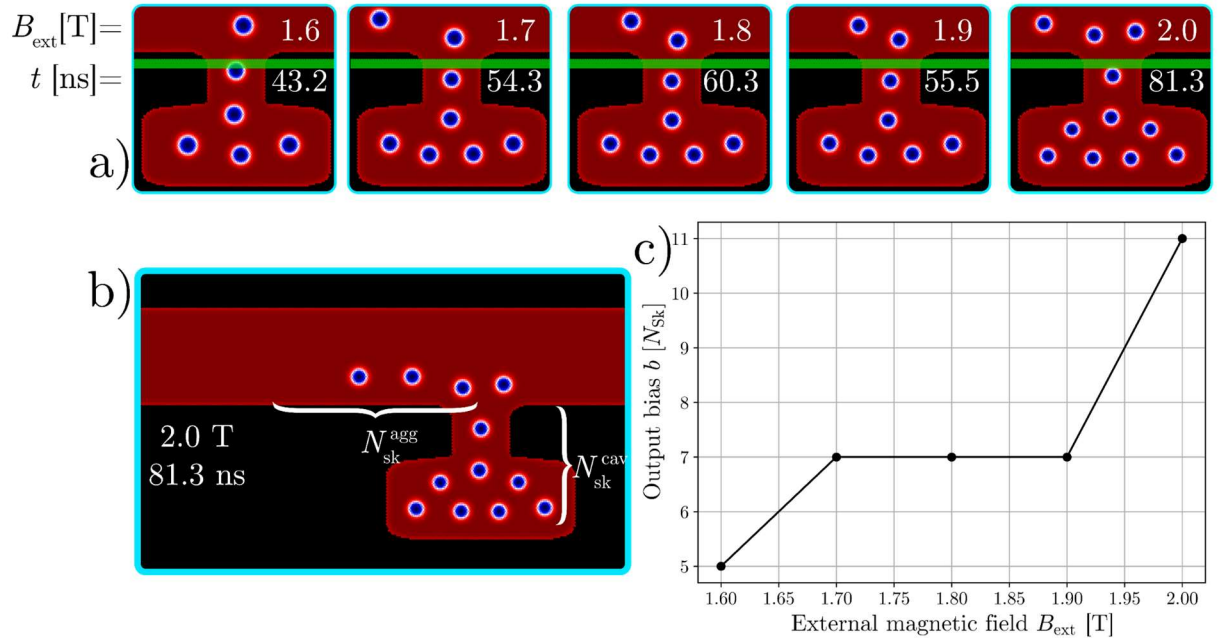


Fig. 17 Analysis of the ReLU behavior analogous to Fig. 16, but for the upper region of $B_{\text{ext}} = [1.6, 2.0]$ T. The bias can be modified within the range $b = [5, 11]$ skyrmions.

Between 1.7 T and 1.9 T, the top skyrmion sits lower as B_{ext} increases (s. green lines in Fig. 17 as a reference). Since $N_{\text{Sk}}^{\text{agg}}$ is 0 at 1.7 T, the bias does not decrease when raising B_{ext} to 1.8 T or 1.9 T, contrasting the behavior for the lower range of B_{ext} ([1.1, 1.5] T). When B_{ext} increases to 2.0 T, $N_{\text{sk}}^{\text{cav}}$ jumps from 6 to 8. Based on energy considerations for confined skyrmions,⁸⁴ the skyrmion configuration of $N_{\text{sk}}^{\text{cav}} = 7$ seems to be

energetically unfavorable for this specific cavity size and shape. Above the upper end of this B_{ext} range, the output does not maintain a strict ReLU shape as the skyrmions are annihilated at the edge of the connecting pathway.

From Fig. 16 and Fig. 17 it is evident that $B_{\text{ext}} = [1.1, 1.5]$ T is advantageous for a ReLU functionality. Although $B_{\text{ext}} = [1.6, 2.0]$ T produces a correct ReLU output, the lower range of $B_{\text{ext}} = [1.1, 1.5]$ T is preferable due to the closed-to-linear adjustability.

Furthermore, we have explored the field dependence of the output bias for different current densities. Coming from $|\vec{v}_{s,\text{in}}| = 2.70 m/s (from Fig. 16 and Fig. 17) we chose $|\vec{v}_{s,\text{in}}| = 5.40 m/s and 4.05 m/s, as above $|\vec{v}_{s,\text{in}}| = 5.40 m/s the skyrmions are annihilated at the “dynamic” pinning site.$$$

The results are shown in Fig. 18 compared to $|\vec{v}_{s,\text{in}}| = 2.70 m/s. Clearly $|\vec{v}_{s,\text{in}}| = 2.70$ m/s provides the widest B_{ext} range for ReLU operations. While the bias increases again above $B_{\text{ext}} = 1.6$ T, the other bias vs. B_{ext} curves for higher $|\vec{v}_{s,\text{in}}|$ values do not show a ReLU output in this range at all.$

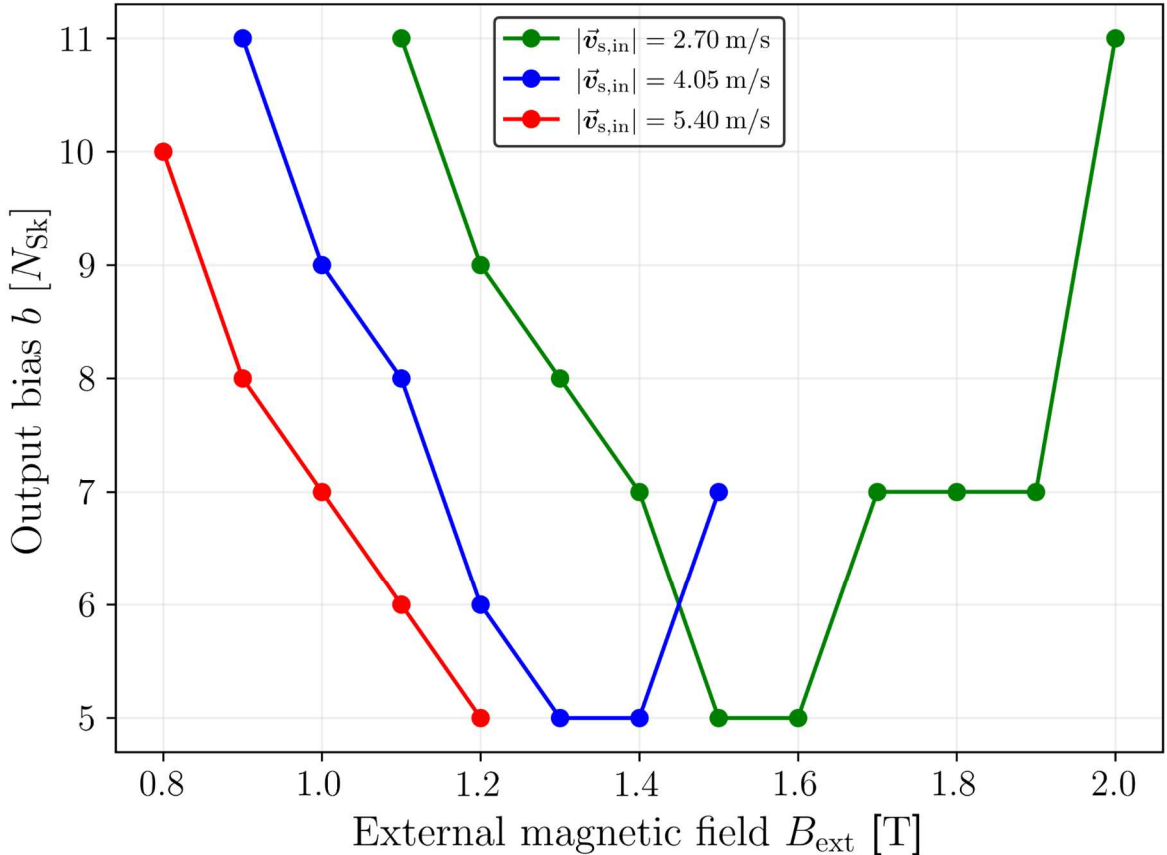


Fig. 18 Graph illustrating the relationship between output bias and B_{ext} across various $|\vec{v}_{s,\text{in}}|$. The race-track and current distribution are the same as in Fig. 15.

The disadvantage of using $|\vec{v}_{s,in}| = 2.70$ m/s is that the total time for a computational operation is higher for lower currents. We can measure this by changing the time between skyrmion creations and observe if the ReLU output changes. The time per skyrmion will be called operational time and decreases drastically from $t_{op} \approx 6.25$ ns/ N_{Sk} to 2.75 ns/ N_{Sk} and 1.75 ns/ N_{Sk} (all ± 0.2 ns/ N_{Sk}) when using a $|\vec{v}_{s,in}|$ of [2.7, 4.05, 5.4] m/s respectively. Therefore, stronger currents could be practicable for computational applications if many skyrmions pass the logic element, as the total power consumption of the racetrack is roughly proportional to $\propto t_{op}/|\vec{v}_{s,in}|$.

7.4.2. Case 2: $\beta > \alpha$

To adapt the racetrack design presented in the preceding chapter for materials where $\beta > \alpha$ we need to modify the design shown in Fig. 15. This adjustment is pertinent because of two primary factors. Firstly, several experimental studies^{24,26,94} have identified high β values for domain-wall movement in magnetic materials (s. chapter 3.2 for further details). Secondly, high β values are associated with reduced t_{op} without necessitating a higher $|\vec{v}_{s,in}|$ and thereby increased efficiencies (s. Fig. 11).

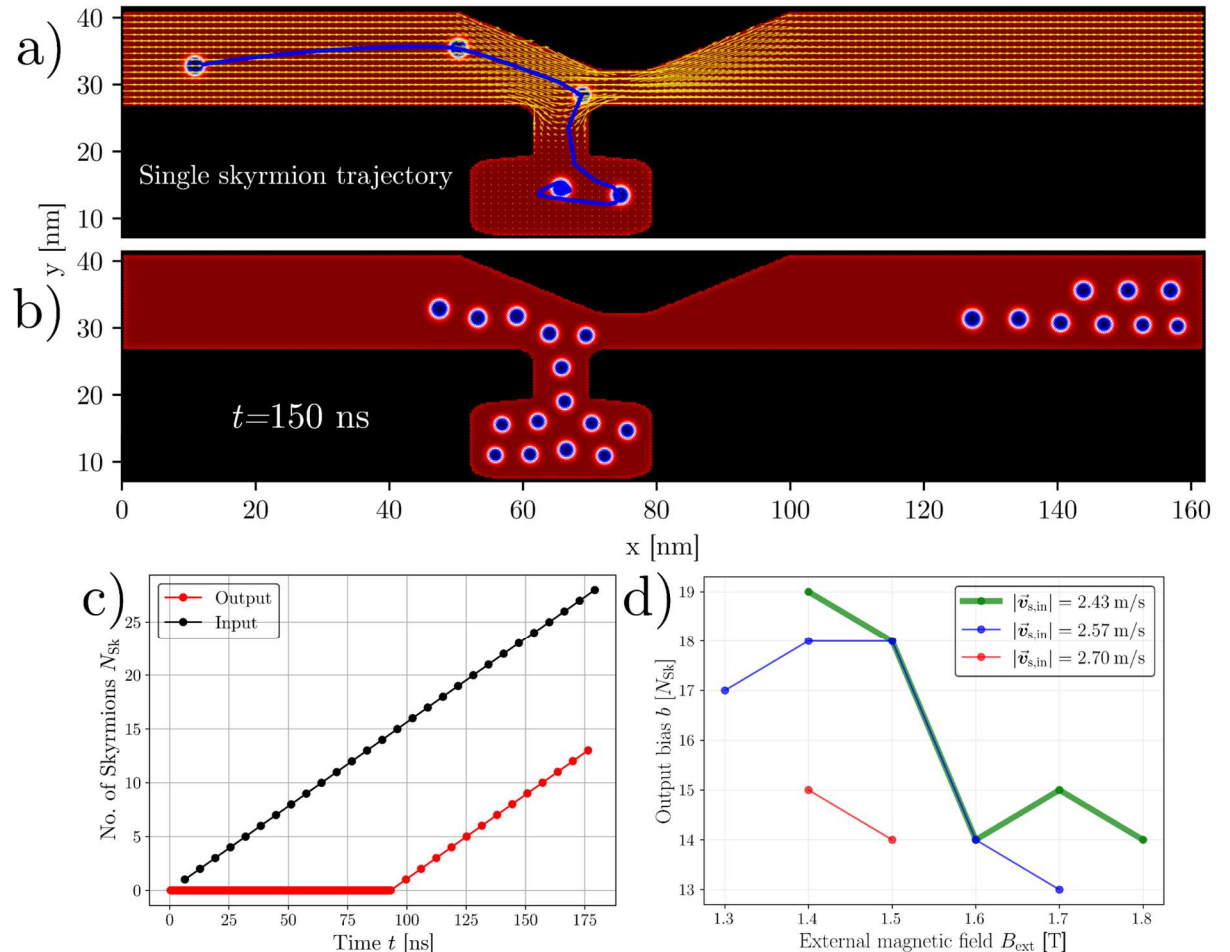


Fig. 19 ReLU racetrack design incorporating a pinch point into the design shown in Fig. 15. The current distribution for $\beta = \alpha \cdot 2$ and $|\vec{v}_{s,in}| = 2.70$ m/s is depicted in **a**). A single skyrmion’s trajectory, given $B_{ext} = 1.5$ T, is shown with exemplary skyrmions at $t = [0,4,5,6,75]$ ns. **b**) shows the magnetic configuration at $t = 150$ ns after skyrmions were generated at the input every 6.4 ns. In **c**), the number of skyrmions generated (input) and the number of skyrmions reaching the output are plotted as a function of time. **d**) illustrates the output bias vs. B_{ext} for different values of $|\vec{v}_{s,in}|$. The ranges of b , $|\vec{v}_{s,in}|$ and B_{ext} are relatively low compared to those shown in Fig. 18 for $\beta = \alpha/2$.

When using the same design as presented in Fig. 15, the skyrmions follow a similar path as shown in Fig. 11 and avoid the cavity. Even when incorporating a cavity at the top of the racetrack, the skyrmions do not get pinned at the “dynamic” pinning site because $\vec{\nu}_{\perp \vec{F}}$ of the pinning site then points toward the output, as it is part of the top edge, not the bottom edge. The most straightforward way to introduce ReLU type behavior for high β values is to incorporate a pinch point where the cavity connects to the racetrack. The modified design and its resulting ReLU behavior are shown in Fig. 19. This ReLU racetrack is only operational in the $|\vec{v}_{s,in}|$ range [2.43, 2.70] m/s. Above this range, the skyrmions are annihilated at the “dynamic” pinning site; below it the current is not strong enough to push them beyond the pinch point. The bias ranges are also less optimal compared to the racetrack and β -value combination shown in Fig. 15, due to the pinch point causing significant dependence on skyrmion size. The minimum operational time is lower for the $\beta > \alpha$ racetrack though, at around $t_{op} \approx 1.25 \pm 0.25$ ns/ N_{Sk} for $|\vec{v}_{s,in}| = 2.57$ m/s.

In conclusion, high β values do not appear to be easily compatible with racetrack designs based on the idea of “dynamic” pinning. Their ReLU output with variable bias shows a narrower bias range and a significantly limited operational $|\vec{v}_{s,in}|$ range. The sole benefit of high β materials is the increased skyrmion drift velocity due to EMD. Consequently, t_{op} is reduced even with a comparatively low input current.

8 Conclusion

We successfully designed and simulated a skyrmion-based ReLU racetrack for $\beta < \alpha$ and demonstrated the potential for implementing non-linear activation functions in neuromorphic computing. In our framework, input and output are the number of skyrmions entering and exiting the racetrack (analog computing). To achieve a ReLU output(input) behavior, we reshaped the edges of the rectangular nanowires (racetracks) traditionally

indented for temporary information storage. By attaching a “cavity” to the racetrack, the skyrmions fill up that cavity first. If enough skyrmions fill up that cavity, they are pushed beyond it by STT and reach the racetrack’s output. This racetrack design only works due to the EMD, leading the skyrmions into the cavity.

The design was slightly modified for $\beta > \alpha$ cases, with the former showing a much wider range of operational parameters. The bias of the ReLU function in our simulations can be adjusted by varying the external magnetic field (\vec{B}_{ext}), offering a tunability that is valuable in neural network applications.

Testing racetracks, we discovered the intrinsic nature of non-perpendicular edge repulsion, which we name the edge Magnus drift (EMD) and the edge repulsion angle $\theta_{\vec{F}}$. After verifying our results with mumax3,^{76,79} we can confidently say that this phenomenon plays a crucial role in skyrmion dynamics within racetracks and has mainly been overlooked^{20,30,87,91} or not recognized in its intrinsic nature^{28,29,86,88,95} in previous studies. The publications that include the EMD have not emphasized it as an inherent property of skyrmions that is relevant without any specific other driving force like a current.

While designing ReLU-racetracks, we established basic guidelines. These include tracking racetrack pinning points and corners. At the same time, we aim for simple designs and consistency of the outcome regarding material parameters, input current, and design changes.

Skyrmion pinning can occur due to various factors, including the material parameters listed in Tab. 1 (chapter 6.1), racetrack geometry (pinch points and sharp corners), and the applied polarized spin polarized current’s strength. We can strategically manipulate these additive factors to achieve desired outcomes in racetrack designs.

The non-adiabatic to adiabatic spin-transfer torque ratio also greatly influences skyrmion trajectories, drift velocities, and pinning potential. Materials with $\beta > \alpha$ are generally favored for faster operational speeds, but they present challenges in racetrack design for computational structures.

Our simulation results all rely on the topological charge only. Therefore, the vorticity and helicity of the skyrmion do not matter for the outcome of our simulations. When simulating skyrmions with $N_{\text{Sk}} = -1$ the non-adiabatic components $\vec{\nu}_{\perp\vec{F}}$ and $\vec{\nu}_{\text{SkH}}$ are inverted (eq. (66) and (67)). Therefore, one can invert the y-axis of racetracks used throughout our simulations when making use of skyrmions with $N_{\text{Sk}} = -1$. The results stay the same qualitatively and can easily be converted.

9 Outlook

These findings improve our understanding of skyrmion dynamics and their potential applications in spintronics and neuromorphic computing. They also change past views on edge repulsion, providing insight into the interesting non-perpendicular edge repulsion and functional racetrack design principles. Several promising avenues for future work emerge from this study. However, there is one long overdue research topic regarding any magnetization-related computational structures: the investigation of efficiency gain/loss compared to traditional silicon currently in use. Although highly fascinating from a physics perspective itself, skyrmion movement is often mentioned to be highly efficient and/or happening at ultralow currents already, many times even mentioned in the abstract.^{28,46,96} However, to the best of our knowledge, skyrmion drift efficiency has only been studied in detail compared to DW movement,⁴⁶ which has never been compared to cheaply available CPU/GPUs for any more complex computational applications.

The most crucial next step in continuing the analysis of edge repulsion is to test our findings in the presence of defects and at non-zero temperatures through simulations. Other studies have already introduced defects and temperatures. These functionalities could be adapted to our framework.^{19,27,32} This could be followed up by experiments to validate our simulations' theoretical predictions. Such experimental work would be invaluable in bridging the gap between theoretical models and potential real-world applications.

Another potential for future research lies in exploring the potential existence of two separate current strength regimes that facilitate skyrmion movement beyond pinning sites such as corners or constrictions. The evidence for that lies in Fig. 12, where we observe a distinct current angle ($\varphi_s = 4.9^\circ$) with two separate current strength zones, where the skyrmion is pushed beyond the pinning site.

A third area of exploration could be the relation of the skyrmion's radius and other material parameters to the repulsion angle. In the lower Δ -region of Fig. 10, this angle is not constant, like in the upper Δ -region, and requires further examination. This investigation could yield additional insights into the limits of the Thiele equation and shed light on the skyrmions' behavior near edges, potentially leading to more accurate models of skyrmion dynamics.

In conclusion, this thesis demonstrates the complex physics underlying skyrmion dynamics in confined geometries. In contrast, one crucial study is missing to promise the ability to create viable, functional, and tunable logic elements using skyrmions.

Addressing the mentioned efficiency issue with such a study could lead to revolutionary advancements in computing technology.

10 Bibliography

1. Klar, M. & Schleiss, J. Künstliche Intelligenz im Kontext von Kompetenzen, Prüfungen und Lehr-Lern-Methoden. *Medien. Zeitschrift für Theor. und Prax. der Medien.* **58**, 41–57 (2024).
2. Grüter, C. Der Markt der Large Language Models—Eine Analyse mit ausgewählten empirischen Daten. *repositorium.hs-ruhrwest.de*.
3. Cardarilli, G. C. *et al.* Energy Consumption Saving in Embedded Microprocessors Using Hardware Accelerators. *TELKOMNIKA (Telecommunication Comput. Electron. Control.)* **16**, 1019 (2018).
4. Kim, J. & Park, M. Dynamic Frequency Scaling Regarding Memory for Energy Efficiency of Embedded Systems. *Int. J. Electr. Comput. Eng.* **8**, 1798 (2018).
5. Kim, Y. *et al.* A Novel CNFET SRAM-Based Compute-In-Memory for BNN Considering Chirality and Nanotubes. *Electronics* **13**, 2192 (2024).
6. Huang, Y., Kang, W., Zhang, X., Zhou, Y. & Zhao, W. Magnetic skyrmion-based synaptic devices. *Nanotechnology* **28**, (2017).
7. Song, K. M. *et al.* Skyrmion-based artificial synapses for neuromorphic computing. *Nat. Electron.* **3**, 148–155 (2020).
8. Borders, W. A. *et al.* Analogue spin-orbit torque device for artificial-neural-network-based associative memory operation. *Appl. Phys. Express* **10**, 013007 (2017).
9. Bourianoff, G., Pinna, D., Sitte, M. & Everschor-Sitte, K. Potential implementation of reservoir computing models based on magnetic skyrmions. *AIP Adv.* **8**, (2018).
10. Wadley, P. *et al.* Electrical switching of an antiferromagnet. *Science (80-).* **351**, 587–590 (2016).
11. Mühlbauer, S. *et al.* Skyrmion Lattice in a Chiral Magnet. *Science (80-).* **323**, 915–919 (2009).
12. Nagaosa, N. & Tokura, Y. Topological properties and dynamics of magnetic skyrmions. *Nat. Nanotechnol.* **8**, 899–911 (2013).
13. Romming, N. *et al.* Writing and Deleting Single Magnetic Skyrmions. *Science (80-).* **341**, 636–639 (2013).
14. Jonietz, F. *et al.* Spin transfer torques in MnSi at ultralow current densities. *Science (80-).* **330**, 1648–1651 (2010).
15. Yu, X. Z. *et al.* Skyrmion flow near room temperature in an ultralow current density. *Nat. Commun.* **3**, (2012).
16. Yu, D., Yang, H., Chshiev, M. & Fert, A. Skyrmions-based logic gates in one single nanotrack completely reconstructed via chirality barrier. *Natl. Sci. Rev.* **9**, 34–36 (2022).
17. Kang, W., Huang, Y., Zhang, X., Zhou, Y. & Zhao, W. Skyrmion-Electronics: An Overview and Outlook. *Phys. Rev. Appl.* **104**, 2040–2061 (2016).

18. Zhang, X. *et al.* Skyrmion-electronics: writing, deleting, reading and processing magnetic skyrmions toward spintronic applications. *J. Phys. Condens. Matter* **32**, 143001 (2020).
19. Strobel, R. Dynamik magnetischer Skyrmionen in realistischen Racetracks: Einfluss von Geometrie und Materialfehlern: Dynamics of magnetic skyrmions in realistic racetracks: influence of geometry and material defects. (Universität Hamburg, 2020).
20. Fook, H. T., Gan, W. L., Purnama, I. & Lew, W. S. Mitigation of Magnus Force in Current-Induced Skyrmion Dynamics. *IEEE Trans. Magn.* **51**, 1–4 (2015).
21. Lai, P. *et al.* An Improved Racetrack Structure for Transporting a Skyrmion. *Sci. Rep.* **7**, 1–8 (2017).
22. Woo, S. *et al.* Current-driven dynamics and inhibition of the skyrmion Hall effect of ferrimagnetic skyrmions in GdFeCo films. *Nat. Commun.* **9**, 959 (2018).
23. Fattouhi, M. *et al.* Electric Field Control of the Skyrmion Hall Effect in Piezoelectric-Magnetic Devices. *Phys. Rev. Appl.* **16**, 1 (2021).
24. Hayashi, M. *et al.* Current driven domain wall velocities exceeding the spin angular momentum transfer rate in permalloy nanowires. *Phys. Rev. Lett.* **98**, 1–4 (2007).
25. Thomas, L., Moriya, R., Rettner, C. & Parkin, S. S. P. Dynamics of magnetic domain walls under their own inertia. *Science (80-.).* **330**, 1810–1813 (2010).
26. Moriya, R. *et al.* Probing vortex-core dynamics using current-induced resonant excitation of a trapped domain wall. *Nat. Phys.* **4**, 368–372 (2008).
27. Jiang, W. *et al.* Direct observation of the skyrmion Hall effect. *Nat. Phys.* **13**, 162–169 (2017).
28. Iwasaki, J., Mochizuki, M. & Nagaosa, N. Current-induced skyrmion dynamics in constricted geometries. *Nat. Nanotechnol.* **8**, 742–747 (2013).
29. Iwasaki, J., Koshiba, W. & Nagaosa, N. Colossal spin transfer torque effect on skyrmion along the edge. *Nano Lett.* **14**, 4432–4437 (2014).
30. Martinez, J. C., Lew, W. S., Gan, W. L. & Jalil, M. B. A. Theory of current-induced skyrmion dynamics close to a boundary. *J. Magn. Magn. Mater.* **465**, 685–691 (2018).
31. Nair, V. & Hinton, G. E. Rectified linear units improve Restricted Boltzmann machines. in *ICML 2010 - Proceedings, 27th International Conference on Machine Learning* 807–814 (2010).
32. Matthies, T. Nutzung von künstlicher Intelligenz für die Erkennung von chiralen magnetischen Strukturen. (Universität Hamburg, 2021).
33. Koziol, M. J. Reevaluation and correction of Maxwell's Equations: a magnetic field has a source, a moving electric charge. *F1000Research* **9**, 1092 (2020).
34. Prasad, R. *Physics and Technology for Engineers. Physics and Technology for Engineers* (Springer Nature Switzerland, Cham, 2023). doi:10.1007/978-3-031-32084-2.
35. Strungaru, M. S. Advanced atomistic models for magnetisation dynamics.

- (University of York, 2020).
- 36. Heisenberg, W. Zur Theorie des Ferromagnetismus, 1928. *Z. Phys* **49**, 619.
 - 37. Cullity, B. D. & Graham, C. D. *Introduction to Magnetic Materials*. (2011).
 - 38. Pauli, W. The Connection Between Spin and Statistics. *Phys. Rev.* **58**, 716–722 (1940).
 - 39. Néel, M. L. Propriétés magnétiques des ferrites ; ferrimagnétisme et antiferromagnétisme. *Ann. Phys. (Paris)* **12**, 137–198 (1948).
 - 40. Dzyaloshinsky, I. A thermodynamic theory of “weak” ferromagnetism of antiferromagnetics. *J. Phys. Chem. Solids* **4**, 241–255 (1958).
 - 41. Moriya, T. Anisotropic Superexchange Interaction and Weak Ferromagnetism. *Phys. Rev.* **120**, 91 (1960).
 - 42. Heesing, C. Einfluss der Dzyaloshinskii-Moriya-Wechselwirkung auf magnetische Moleküle. (Universität Bielefeld, 2016).
 - 43. Zeeman, P. XXXII. On the influence of magnetism on the nature of the light emitted by a substance. *London, Edinburgh, Dublin Philos. Mag. J. Sci.* **43**, 226–239 (1897).
 - 44. Skyrme, T. H. R. A unified field theory of mesons and baryons. *Nucl. Phys.* **31**, 556–569 (1962).
 - 45. Heinze, S. *et al.* Spontaneous atomic-scale magnetic skyrmion lattice in two dimensions. *Nat. Phys.* **7**, 713–718 (2011).
 - 46. Fert, A., Cros, V. & Sampaio, J. Skyrmions on the track. *Nat. Nanotechnol.* **8**, 152–156 (2013).
 - 47. Wang, X. S., Yuan, H. Y. & Wang, X. R. A theory on skyrmion size. *Commun. Phys.* **1**, 1–7 (2018).
 - 48. Braun, H. B. Fluctuations and instabilities of ferromagnetic domain-wall pairs in an external magnetic field. *Phys. Rev. B* **50**, 16485–16500 (1994).
 - 49. Krüger, B. Current-driven magnetization dynamics: Analytical modeling and numerical simulation dissertation. *PhD Thesis* (2011).
 - 50. Drews, A. Dynamics of magnetic vortices and antivortices. *PhD Thesis* (2009).
 - 51. Slonczewski, J. C. Current-driven excitation of magnetic multilayers. *J. Magn. Magn. Mater.* **159**, L1–L7 (1996).
 - 52. Berger, L. Emission of spin waves by a magnetic multilayer traversed by a current. *Phys. Rev. B* **54**, 9353–9358 (1996).
 - 53. Bazaliy, Y. B., Jones, B. & Zhang, S. C. Modification of the Landau-Lifshitz equation in the presence of a spin-polarized current in colossal- and giant-magnetoresistive materials. *Phys. Rev. B - Condens. Matter Mater. Phys.* **57**, R3213–R3216 (1998).
 - 54. Zhang, S. & Li, Z. Roles of nonequilibrium conduction electrons on the magnetization dynamics of ferromagnets. *Phys. Rev. Lett.* **93**, 1–4 (2004).
 - 55. Schütte, C., Iwasaki, J., Rosch, A. & Nagaosa, N. Inertia, diffusion, and dynamics of a driven skyrmion. *Phys. Rev. B - Condens. Matter Mater. Phys.* **90**, (2014).

56. Thiele, A. A. Steady-state motion of magnetic domains. *Phys. Rev. Lett.* **30**, 230–233 (1973).
57. Everschor, K. Current-induced dynamics of chiral magnetic structures. *Thesis* (Universität zu Köln, 2012).
58. Everschor, K. *et al.* Rotating skyrmion lattices by spin torques and field or temperature gradients. *Phys. Rev. B - Condens. Matter Mater. Phys.* **86**, (2012).
59. Schwarz, H.-R. & Köckler, N. *Numerische Mathematik*. (Springer-Verlag, 2013).
60. Munz, C.-D. & Westermann, T. *Numerische Behandlung Gewöhnlicher Und Partieller Differenzialgleichungen. Numerische Behandlung gewöhnlicher und partieller Differenzialgleichungen* (2019). doi:10.1007/978-3-662-55886-7.
61. Jordan, M. I. & Mitchell, T. M. Machine learning: Trends, perspectives, and prospects. *Science (80-).* **349**, 255–260 (2015).
62. Shi, Y. Research on the Stock Price Prediction Using Machine Learning. *Adv. Econ. Manag. Polit. Sci.* **22**, 174–179 (2023).
63. McKinney, B. A., Reif, D. M., Ritchie, M. D. & Moore, J. H. Machine Learning for Detecting Gene-Gene Interactions. *Appl. Bioinformatics* **5**, 77–88 (2006).
64. Đaković, D., Kljajić, M., Milivojević, N., Doder, Đ. & Andelković, A. S. Review of Energy-Related Machine Learning Applications in Drying Processes. *Energies* **17**, 224 (2023).
65. Gheibi, O., Weyns, D. & Quin, F. Applying Machine Learning in Self-adaptive Systems. *ACM Trans. Auton. Adapt. Syst.* **15**, 1–37 (2020).
66. Urban, C. & Gates, K. Deep Learning: A Primer for Psychologists. (2019) doi:10.31234/OSF.IO/4Q8NA.
67. Aggarwal, C. C. Neural Networks and Deep Learning. *Neural Networks Deep Learn.* (2018) doi:10.1007/978-3-319-94463-0.
68. Geman, S., Bienenstock, E. & Doursat, R. Neural Networks and the Bias/Variance Dilemma. *Neural Comput.* **4**, 1–58 (1992).
69. Hu, Z., Zhang, J. & Ge, Y. Handling Vanishing Gradient Problem Using Artificial Derivative. *IEEE Access* **9**, 22371–22377 (2021).
70. Ven, L. & Lederer, J. Regularization and Reparameterization Avoid Vanishing Gradients in Sigmoid-Type Networks. (2021) doi:10.48550/arXiv.2106.02260.
71. Werbos, P. J. Backpropagation through time: what it does and how to do it. *Proc. IEEE* **78**, 1550–1560 (1990).
72. LeCun, Y., Bottou, L., Bengio, Y. & Haffner, P. Gradient-based learning applied to document recognition. *Proc. IEEE* **86**, 2278–2323 (1998).
73. Lin, H. W., Tegmark, M. & Rolnick, D. Why Does Deep and Cheap Learning Work So Well? *J. Stat. Phys.* **168**, 1223–1247 (2017).
74. Smith, L. N. Cyclical Learning Rates for Training Neural Networks. in *2017 IEEE Winter Conference on Applications of Computer Vision (WACV)* 464–472 (IEEE, 2017). doi:10.1109/WACV.2017.58.
75. Wang, W., Xu, L. & Yang, L.-P. Towards a Fire Alarm Model Based on Variable

- Learning Rate Algorithm with Weight Factor. *Proc. 2014 Int. Conf. Mechatronics, Control Electron. Eng.* **113**, 103–106 (2014).
76. Kettner, A. Python Micromagnetic Framework. at <https://github.com/AntonKettner/PyMMF> (2024).
77. Braun, H.-B. Topological effects in nanomagnetism: from superparamagnetism to chiral quantum solitons. *Adv. Phys.* **61**, 1–116 (2012).
78. Mitsui, T. & Hu, G.-D. *Numerische Analyse von Gewöhnlichen Und Retardierten Differentialgleichungen*. arxiv.org (Springer Nature Singapore, Singapore, 2024). doi:10.1007/978-981-99-7974-5.
79. Vansteenkiste, A. *et al.* The design and verification of MuMax3. *AIP Adv.* **4**, (2014).
80. Spethmann, J., Vedmedenko, E. Y., Wiesendanger, R., Kubetzka, A. & von Bergmann, K. Zero-field skyrmionic states and in-field edge-skyrmions induced by boundary tuning. *Commun. Phys.* **5**, 19 (2022).
81. Romming, N., Kubetzka, A., Hanneken, C., Von Bergmann, K. & Wiesendanger, R. Field-dependent size and shape of single magnetic Skyrmions. *Phys. Rev. Lett.* **114**, 1–5 (2015).
82. Hagemeister, J., Siemens, A., Rózsa, L., Vedmedenko, E. Y. & Wiesendanger, R. Controlled creation and stability of $k\pi$ skyrmions on a discrete lattice. *Phys. Rev. B* **97**, 1–7 (2018).
83. Dupé, B., Hoffmann, M., Paillard, C. & Heinze, S. Tailoring magnetic skyrmions in ultra-thin transition metal films. *Nat. Commun.* **5**, 1–6 (2014).
84. Schäffer, A. F., Rózsa, L., Berakdar, J., Vedmedenko, E. Y. & Wiesendanger, R. Stochastic dynamics and pattern formation of geometrically confined skyrmions. *Commun. Phys.* **2**, 1–10 (2019).
85. Lin, S. Z., Batista, C. D. & Saxena, A. Internal modes of a skyrmion in the ferromagnetic state of chiral magnets. *Phys. Rev. B - Condens. Matter Mater. Phys.* **89**, 1–7 (2014).
86. Garcia-Sánchez, F., Sampaio, J., Reyren, N., Cros, V. & Kim, J. V. A skyrmion-based spin-torque nano-oscillator. *New J. Phys.* **18**, 1–10 (2016).
87. Martinez, J. C. & Jalil, M. B. A. Topological dynamics and current-induced motion in a skyrmion lattice. *New J. Phys.* **18**, (2016).
88. Göbel, B. & Mertig, I. Skyrmion ratchet propagation: utilizing the skyrmion Hall effect in AC racetrack storage devices. *Sci. Rep.* **11**, 1–11 (2021).
89. Wang, C., Xiao, D., Chen, X., Zhou, Y. & Liu, Y. Manipulating and trapping skyrmions by magnetic field gradients. *New J. Phys.* **19**, (2017).
90. Yanes, R. *et al.* Skyrmion motion induced by voltage-controlled in-plane strain gradients. *Appl. Phys. Lett.* **115**, 1–6 (2019).
91. Zhang, X. *et al.* Skyrmion-skyrmion and skyrmion-edge repulsions in skyrmion-based racetrack memory. *Sci. Rep.* **5**, 1–6 (2015).
92. Fukushima, K. Visual Feature Extraction by a Multilayered Network of Analog

- Threshold Elements. *IEEE Trans. Syst. Sci. Cybern.* **5**, 322–333 (1969).
- 93. Siemens, A., Zhang, Y., Hagemeyer, J., Vedmedenko, E. Y. & Wiesendanger, R. Minimal radius of magnetic skyrmions: Statics and dynamics. *New J. Phys.* **18**, (2016).
 - 94. Thomas, L. *et al.* Oscillatory dependence of current-driven magnetic domain wall motion on current pulse length. *Nature* **443**, 197–200 (2006).
 - 95. Zhang, X. *et al.* All-magnetic control of skyrmions in nanowires by a spin wave. *Nanotechnology* **26**, 1–8 (2015).
 - 96. Chen, G. Skyrmion Hall effect. *Nat. Phys.* **13**, 112–113 (2017).
 - 97. Zhang, H., Zhu, D., Kang, W., Zhang, Y. & Zhao, W. Stochastic Computing Implemented by Skyrmionic Logic Devices. *Phys. Rev. Appl.* **13**, 1 (2020).

Declaration of Academic integrity

I hereby solemnly declare that I have written the present thesis on my own, have not used any other aids or sources than those indicated and that it has not been submitted in any form for another degree at any university or other institute.

Insofar as generative Artificial Intelligence (gAI) based electronic aids were used in the preparation of the present thesis, I declare that my own contribution remains predominant and that a complete documentation of all used aids is available in accordance with good scientific practice. I bear the responsibility for any faulty or distorted content generated by the gAI, incorrect references, violations of data protection and copyright laws, or plagiarism.

Hamburg, 03.07.2024,

A handwritten signature in black ink, appearing to read "A. Kettner". It is written in a cursive style with a horizontal line underneath it.

Place, Date, Signature

11 Appendix

11.1 Drift speed and angle in relation to the current and β

In this part of the appendix, we will showcase two basic properties of the observed skyrmions, firstly:

$$|\vec{\nu}_{\text{STT}}| = a \cdot |\vec{v}_s|. \quad (71)$$

This relationship is illustrated in Fig. 20 a) and c).

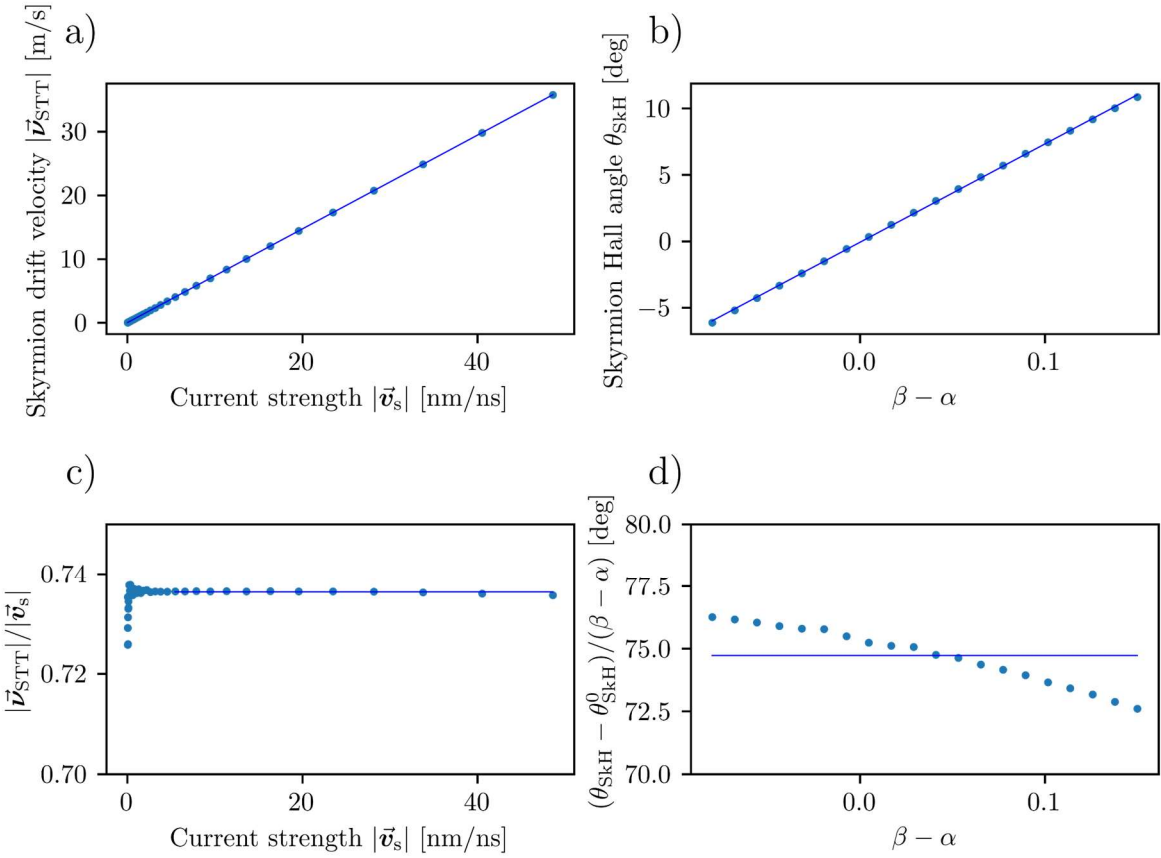


Fig. 20 a) c) Plots of $|\vec{\nu}_{\text{STT}}|$, and $|\vec{\nu}_{\text{STT}}|/|\vec{v}_s|$ against the current strengths $|\vec{v}_s|$. b) d) Plots of θ_{SkH} and $(\theta_{\text{SkH}} - \theta_{\text{SkH}}^0)/(\beta - \alpha)$ against $\beta - \alpha$ with $\alpha = 0.1$ and $\vec{v}_s = \frac{10}{s} \text{ m}$. In figures a) and b), the data is fitted with a linear equation, whereas in figures c) and d), a constant value is used for fitting. The fit in c) is done for $|\vec{v}_s| > 5$ m/s.

In c) it can be seen that $|\vec{\nu}_{\text{STT}}|$ has a roughly linear relation to $|\vec{v}_s|$ for $|\vec{v}_s| > 5$ m/s, leading to a fit of $|\vec{\nu}_{\text{STT}}|/|\vec{v}_s| = a = 0.736$ with $\sigma = 0.00023$.

Secondly, with $\theta_{\text{SkH}}^0 = 0.0024$ determined in Fig. 5 inside chapter 5.1.3 and given the visually linear relationship seen in Fig. 20 b) one could assume:

$$\theta_{\text{SkH}} = a \cdot (\beta - \alpha) + \theta_{\text{SkH}}^0, \quad (72)$$

d) shows that θ_{SkH} does not change linearly with β though. Fitting with a constant value is not only visually wrong but also leads to a standard deviation of $\sigma = 1.21^\circ$, far too large to be acceptable.

11.2 Derivation of the skyrmion velocity from the Thiele equation

This chapter shows the reorganization of eq. (30) into the full motion equation (34), separating the velocity of the skyrmion $\vec{\nu}$. Hereby we make use of \vec{G} not containing x- and y-components (s. eq. (31)) and the diagonalized version of \vec{D} only its eigenvalues at $D_{xx} = D_{yy} = D$ (s. eq. (33)). Written in a vector format we get:

$$0 = \begin{pmatrix} 0 \\ 0 \\ G \end{pmatrix} \times \left(\begin{pmatrix} \nu_x \\ \nu_y \\ 0 \end{pmatrix} - \begin{pmatrix} v_{s,x} \\ v_{s,y} \\ 0 \end{pmatrix} \right) + \begin{pmatrix} D & 0 & 0 \\ 0 & D & 0 \\ 0 & 0 & 0 \end{pmatrix} \left(\alpha \begin{pmatrix} \nu_x \\ \nu_y \\ 0 \end{pmatrix} - \beta \begin{pmatrix} v_{s,x} \\ v_{s,y} \\ 0 \end{pmatrix} \right) + \begin{pmatrix} F_x \\ F_y \\ F_z \end{pmatrix}. \quad (73)$$

This can be simplified into,

$$\begin{pmatrix} -G \cdot (\nu_y - v_{s,x}) \\ G \cdot (\nu_x - v_{s,y}) \\ 0 \end{pmatrix} + D \cdot \begin{pmatrix} \alpha \cdot \nu_x - \beta \cdot v_{s,x} \\ \alpha \cdot \nu_y - \beta \cdot v_{s,y} \\ 0 \end{pmatrix} + \begin{pmatrix} F_x \\ F_y \\ F_z \end{pmatrix} = 0, \quad (74)$$

and can be written into two equations:

$$-G \cdot (\nu_y - v_{s,x}) + D \cdot (\alpha \cdot \nu_x - \beta \cdot v_{s,x}) + F_x = 0, \quad (75)$$

$$G \cdot (\nu_x - v_{s,y}) + D \cdot (\alpha \cdot \nu_y - \beta \cdot v_{s,y}) + F_y = 0. \quad (76)$$

Reformulating eq. (75) to separate ν_x and (76) to separate ν_y ,

$$\nu_x = \frac{\beta D \cdot v_{s,x} + G(\nu_y - v_{s,y}) - F_x}{\alpha D}, \quad (77)$$

$$\nu_y = \frac{\beta D \cdot v_{s,y} - G(\nu_x - v_{s,x}) - F_y}{\alpha D}, \quad (78)$$

and inserting (77) into (78):

$$\nu_y = \frac{\beta D \cdot v_{s,y} - G \left(\frac{\beta D \cdot v_{s,x} + G(\nu_y - v_{s,y}) - F_x}{\alpha D} - v_{s,x} \right) - F_y}{\alpha D}. \quad (79)$$

Afterward expressing all the terms as numerators of the denominator $\alpha^2 D^2$,

$$\nu_y = \frac{\alpha \beta D^2 v_{s,y} - \beta G D v_{s,x} + G^2 v_{s,y} - G^2 \nu_y + G F_x + \alpha D G v_{s,x} - \alpha D F_y}{\alpha^2 D^2}, \quad (80)$$

separating ν_y ,

$$\nu_y = \frac{\alpha \beta D^2 v_{s,y} - \beta G D v_{s,x} + G^2 v_{s,y} - G F_x + \alpha D G v_{s,x} - \alpha D F_y}{\alpha^2 D^2 \cdot \left(1 + \frac{G^2}{\alpha^2 D^2} \right)}, \quad (81)$$

and simplifying again yields:

$$\nu_y = \frac{(\alpha \beta D^2 + G^2) \cdot v_{s,y} + G D (\alpha - \beta) \cdot v_{s,x} - G \cdot F_x - \alpha D \cdot F_y}{\alpha^2 D^2 + G^2}. \quad (82)$$

To obtain ν_x we instead insert eq. (78) into (77),

$$\nu_x = \frac{\beta D \cdot v_{s,x} + G \left(\frac{\beta D \cdot v_{s,y} - G(\nu_x - v_{s,x}) - F_y}{\alpha D} - v_{s,y} \right) - F_x}{\alpha D}, \quad (83)$$

and express all the terms as numerators of the denominator $\alpha^2 D^2$ again,

$$\nu_x = \frac{\alpha \beta D^2 v_{s,x} + \beta G D v_{s,y} - G^2 (\nu_x - v_{s,x}) - G F_y - \alpha G D v_{s,y} - \alpha D F_x}{\alpha^2 D^2}, \quad (84)$$

separate ν_x and simplify like before, yielding:

$$\nu_x = \frac{(\alpha\beta D^2 + G^2) \cdot v_{s,x} - GD(\alpha - \beta) \cdot v_{s,y} - GF_y - \alpha DF_x}{\alpha^2 D^2 + G^2} \quad (85)$$

Eq. (82) and (85) can be put into one vector equation, dividing into a collinear and an orthogonal part:

$$\begin{aligned} \vec{\nu} &= \frac{1}{G^2 + \alpha^2 D^2} \\ &\cdot \left(-\alpha D \vec{F} + \begin{pmatrix} -GF_y \\ GF_x \\ 0 \end{pmatrix} + (\alpha\beta D^2 + G^2) \cdot \vec{v}_s + (\alpha - \beta) D \begin{pmatrix} -Gv_{s,y} \\ Gv_{s,x} \\ 0 \end{pmatrix} \right) \end{aligned} \quad (86)$$

Considering the cross-product $\vec{G} \times \vec{F}$ and $\vec{G} \times \vec{v}_s$,

$$\vec{G} \times \vec{F} = \begin{pmatrix} 0 \\ 0 \\ G \end{pmatrix} \times \begin{pmatrix} F_x \\ F_y \\ F_z \end{pmatrix} = \begin{pmatrix} -GF_y \\ GF_x \\ 0 \end{pmatrix}, \quad (87)$$

$$\vec{G} \times \vec{v}_s = \begin{pmatrix} 0 \\ 0 \\ G \end{pmatrix} \times \begin{pmatrix} v_{s,x} \\ v_{s,y} \\ 0 \end{pmatrix} = \begin{pmatrix} -Gv_{s,y} \\ v_{s,x} \\ 0 \end{pmatrix}, \quad (88)$$

eq. (86) simplifies into the full motion equation (34) in chapter 4.3.3.

11.3 Derivation of $\phi \approx \bar{\phi}_{NN}$

To derive eq. (58) from the Laplace equation (41), we can approximate the electrical potential at neighboring sites $\phi_{\vec{r} + \vec{g}_{NN}}$ with,

$$T_2(\phi_{\vec{r} + \vec{g}_{NN}}) = \phi_{\vec{r}} + \vec{g}_{NN} \cdot \vec{\nabla} \phi_{\vec{r}} + \frac{\vec{g}_{NN}^T}{2} \cdot \vec{\mathbf{H}}_{\phi_{\vec{r}}}(\vec{r}) \cdot \vec{g}_{NN} + \mathcal{O}(h^3), \quad (89)$$

\vec{g}_{NN} being the vector pointing toward the specific NN, \vec{r} and $\vec{r} + \vec{g}_{NN}$ denoting the vector toward a specific site and the vector pointing toward the respective NN, and $\vec{\mathbf{H}}_{\phi_{\vec{r}}}(\vec{r})$ being the Hesse matrix of ϕ at site \vec{r} . Summing over all NN potentials yields:

$$\sum_{\vec{g}_{NN}}^{NN} \phi_{\vec{r} + \vec{g}_{NN}} \approx \sum_{\vec{g}_{NN}}^{NN} \left(\phi_{\vec{r}} + \vec{g}_{NN} \cdot \vec{\nabla} \phi_{\vec{r}} + \frac{\vec{g}_{NN}^T}{2} \cdot \vec{\mathbf{H}}_{\phi_{\vec{r}}}(\vec{r}) \cdot \vec{g}_{NN} \right) \quad (90)$$

In the following few equations, I will show that the quadratic term is zero here, considering we have evenly spaced N vectors \vec{g}_{NN} over the unit circle.

Due to trace $(\vec{\mathbf{H}}_{\phi_{\vec{r}}}(\vec{r})) = 0$ we have:

$$\vec{\mathbf{H}}_{\phi_{\vec{r}}}(\vec{r}) = \begin{pmatrix} a & b \\ b & -a \end{pmatrix} \quad (91)$$

Considering that,

$$\vec{g}_{NN}^T \cdot \vec{\mathbf{H}}_{\phi_{\vec{r}}}(\vec{r}) \cdot \vec{g}_{NN} = |\vec{g}_{NN}|^2 \cdot \vec{e}_{NN}^T \cdot \vec{\mathbf{H}}_{\phi_{\vec{r}}}(\vec{r}) \cdot \vec{e}_{NN} \quad (92)$$

we can write the unit vectors \vec{e}_{NN} as,

$$\vec{e}_{NN} = \begin{pmatrix} \cos(\theta) \\ \sin(\theta) \end{pmatrix}, \quad (93)$$

and the product $\vec{e}_{NN}^T \cdot \vec{\mathbf{H}}_{\phi_{\vec{r}}}(\vec{r}) \cdot \vec{e}_{NN}$ as,

$$\vec{e}_{NN}^T \cdot \vec{\mathbf{H}}_{\phi_{\vec{r}}}(\vec{r}) \cdot \vec{e}_{NN} = (\cos(\theta) \quad \sin(\theta)) \begin{pmatrix} a & b \\ b & -a \end{pmatrix} \begin{pmatrix} \cos(\theta) \\ \sin(\theta) \end{pmatrix}, \quad (94)$$

Simplifying to:

$$\vec{e}_{NN}^T \cdot \vec{\mathbf{H}}_{\phi_{\vec{r}}}(\vec{r}) \cdot \vec{e}_{NN} = a \cdot \cos 2\theta + b \cdot \sin 2\theta. \quad (95)$$

With the angles being evenly spaced in the 2D plane we can state $\theta_i = \frac{2k\pi}{N}$, $k = 0, 1, 2, \dots, N-1$ and with that reformulate the sum over N_{NN} vectors \vec{g}_{NN} as:

$$\sum_{k=0}^{N-1} (a \cdot \cos 2\theta_k + b \cdot \sin 2\theta_k). \quad (96)$$

As both terms are zero with evenly spaced θ_k , the quadratic term is zero:

$$\sum_{\vec{g}_{NN}}^{NN} (\phi_{\vec{r}} + \vec{g}_{NN} \cdot \vec{\nabla} \phi_{\vec{r}}). \quad (97)$$

The second term is zero for the same reason, the vectors being evenly spaced in a circle,

$$\sum_{\vec{g}_{NN}}^{NN} \vec{g}_{NN} \cdot \vec{\nabla} \phi_{\vec{r}} = \vec{\nabla} \phi_{\vec{r}} \sum_{\vec{g}_{NN}}^{NN} \vec{g}_{NN} = 0, \quad (98)$$

Therefore:

$$\overline{\phi}_{\vec{g}_{NN}} = No_{NN}^{-1} \cdot \sum_{\vec{g}_{NN}}^{NN} \phi_{\vec{r} + \vec{g}_{NN}} \approx No_{NN} \cdot \sum_{\vec{g}_{NN}}^{NN} \phi_{\vec{r}} = \overline{\phi}_{\vec{r}} = \phi_{\vec{r}}. \quad (99)$$